Conformational transitions and ligand-binding to a muscle-type nicotinic acetylcholine receptor

Eleftherios Zarkadas, Eva Pebay-Peyroula, Mackenzie John Thompson, Guy Schoehn, Tomasz Uchański, Jan Steyaert, Christophe Chipot, Francois Dehez, John Edward Baenziger, Hugues Nury

Eleftherios Zarkadas, Eva Pebay-Peyroula, Mackenzie John Thompson, Guy Schoehn, Tomasz Uchański, et al.. Conformational transitions and ligand-binding to a muscle-type nicotinic acetylcholine receptor. Neuron, 2022, 110 (8), pp.1358-1370.e5. ⟨10.1016/j.neuron.2022.01.013⟩. ⟨hal-04893282⟩

Version of Record: https://www.sciencedirect.com/science/article/pii/S0896627322000496
Manuscript_638c58053648bb8533b1af21cef4b18e

Conformational transitions and ligand-binding to a muscle-type nicotinic acetylcholine receptor

Eleftherios Zarkadas[1], Eva Pebay-Peyroula[1], Mackenzie John Thompson[2], Guy Schoehn[1], Tomasz Uchański[6-7], Jan Steyaert[6-7], Christophe Chipot[3-5], Francois Dehez[3,4], John Edward Baenziger[2,8,*], Hugues Nury[1,*]

1. Univ. Grenoble Alpes, CNRS, CEA, IBS, F-38000 Grenoble, France
2. Department of Biochemistry, Microbiology and Immunology, University of Ottawa, Ottawa, Ontario, Canada
3. Université de Lorraine, CNRS, LPCT, F-54000 Nancy, France
4. Laboratoire International Associé CNRS and University of Illinois at Urbana−Champaign, Vandoeuvre-les-Nancy, France
5. Department of Physics, University of Illinois at Urbana−Champaign, Urbana, Illinois, USA
6. Structural Biology Brussels, Vrije Universiteit Brussel, Brussels, Belgium
7. VIB-VUB Center for Structural Biology, VIB, Brussels, Belgium
8. Further information and requests for resources and reagents should be directed to and will be fulfilled by the lead contact, John Baenziger (john.baenziger@uottawa.ca).

*to whom correspondence should be addressed: hugues.nury@ibs.fr or john.baenziger@uottawa.ca

Fast synaptic communication requires receptors that respond to the presence of neurotransmitter by opening an ion channel across the post-synaptic membrane. The muscle-type nicotinic acetylcholine receptor from the electric fish, *Torpedo*, is the prototypic ligand-gated ion channel, yet the structural changes underlying channel activation remain undefined. Here we use cryo-EM to solve apo and agonist-bound structures of the *Torpedo* nicotinic receptor embedded in a lipid nanodisc. Using both a direct biochemical assay to define the conformational landscape and molecular dynamics simulations to assay flux through the pore, we correlate structures with functional states and elucidate the motions that lead to pore activation of a heteromeric nicotinic receptor. We highlight an underappreciated role for the complementary subunit in channel gating, establish the structural basis for the differential agonist affinities of □/□ versus □ /□ sites and explain why nicotine is less potent at muscle nicotinic receptors compared to neuronal ones.

Introduction

Nicotinic acetylcholine receptors (nAChRs) mediate fast synaptic communication at neuronal synapses and neuromuscular junctions, are implicated in a plethora of neurological disorders and play a central role in nicotine addiction. nAChRs have been the subject of scrutiny since the early twentieth century discovery that muscle contains a receptive substance that binds nicotine and elicits its postsynaptic response (Langley, 1905). The subsequent discovery that the electric organ from *Torpedo* is an abundant source of this nicotine receptive substance led to the eventual identification of the muscle-type nAChR (Changeux, 2012). The *Torpedo* nAChR is the prototypic member of a superfamily of pentameric ligand-gated ion channels (pLGICs) that includes both muscle and neuronal nAChRs, as well as serotonin (5-HT3), GABA$_A$ and glycine receptors.

A defining feature of all pLGICs is the temporal nature of the agonist-induced response, which is governed by transitions between conformational states. In the absence of agonist, the nAChR exists predominantly in a closed resting conformation that does not conduct ions across the membrane. When presented with acetylcholine, the nAChR transitions from resting through intermediate states to an open conformation that transiently conducts cations across the membrane (Jadey and Auerbach, 2012; Lape et al., 2008; Mukhtasimova et al., 2009). Prolonged minute-long exposure to acetylcholine leads to the formation of a desensitized conformation(s) that has a high affinity for acetylcholine but a closed pore.

Long before single-particle cryo-electron microscopy (cryo-EM) became the widely practised technique it is today, helical image reconstructions from electron micrographs recorded from crystalline tubes, which self-assemble from native *Torpedo* membranes, established the fundamental pLGIC architecture (Miyazawa et al., 2003; Unwin, 2005) and yielded the first images of the resting to open transition (Unwin and Fujiyoshi, 2012). Since 2015, rapid advancements in cryo-EM have led to an explosive growth of our knowledge of pLGIC structures revealing fine details regarding the binding of drugs (Masiulis et al., 2019), etc., along with diverse snapshots into the conformational landscape (Kumar et al., 2020; Polovinkin et al., 2018; Rovšnik et al., 2020). Neuronal □4□2 and □3□4 nAChRs have been imaged in agonist-bound states (Gharpure et al., 2019; Walsh et al., 2018). In the past two years, three conformations of the □7 nAChR (Noviello et al., 2021) and an inhibited state of the *Torpedo* nAChR (Rahman et al., 2020) have been reported. These new structures, however, have not delivered a unifying picture of how agonist binding transitions a resting pLGIC through its intermediate conformations to open and ultimately desensitized conformations. A factor that hinders our understanding is the difficulty of assigning a given structure to a physiological state. For example, it remains unclear how a lower pore constriction observed in agonist-bound nAChR structures deemed desensitized impairs the permeation of ions (Gielen and Corringer, 2018).

Here, we use the channel pore binding probe, ethidium bromide (EthBr), to directly assess the conformational state of nanodisc-reconstituted *Torpedo* nAChRs and report cryo-EM structures of apo and both carbamylcholine (Carb)- and nicotine-bound states. The three new structures define the structural basis for agonist binding to the two non-equivalent □-□ and □-□ sites, the differential affinities of muscle versus neuronal nAChRs for the addictive alkaloid, nicotine, and the nature of lipid binding. The structures also elucidate the conformational transitions that lead to both increased agonist-affinity and activation of the channel pore.

Results & Discussion

Apo, carbamylcholine and nicotine datasets: a main resting state and a desensitized-like conformation

The nAChR from *Torpedo californica* was affinity purified and reconstituted into both soybean asolectin liposomes and MSP2N2 nanodiscs. To characterize the conformational landscape in both, we measured the binding of EthBr, a fluorescent probe that has low and high affinities, respectively, for the resting (K_D > 1mM) and open/desensitized states (K_D open not defined; K_D desensitized = 0.3-0.85 μM), with EthBr fluorescence increasing ~15-fold upon pore binding (Herz et al., 1987; Sun et al., 2017)). In both membranes, kinetic assays performed in the absence of agonist at 0.3 □M EthBr (Fig. 1a) detect a dibucaine-displaceable fluorescence due to EthBr binding to nAChRs that exist in a high-affinity conformation(s) (~40/~50% in liposomes/nanodiscs). Subsequent addition of Carb leads to a further increase in fluorescence as the nAChR transitions from low to high affinity EthBr binding states (~60/~50% in liposomes/nanodiscs). These kinetic assays demonstrate that the nAChR in both liposomes and nanodiscs exists in an equilibrium between low and high affinity EthBr-binding conformations. Previous studies have shown that the high affinity conformation(s) observed in the absence of agonist has a slower on-rate for EthBr binding than the open nAChR and is thus likely desensitized (daCosta and Baenziger, 2009; daCosta et al., 2013), consistent with the natural equilibrium between resting and desensitized states observed in native *Torpedo* membranes (Boyd and Cohen, 1980). More importantly, the EthBr binding experiments provide the first direct biochemical evidence that a pLGIC in a lipid nanodisc retains the ability to undergo agonist-induced conformational transitions.

CryoEM data sets with no added ligand and with added Carb or nicotine were recorded using the nAChR MSP2N2 nanodiscs (Fig. SI1, SI2, SI3, SI4, Table SI1) in the presence of MSP-targeted megabodies that facilitate an isotropic distribution of particle orientations (Uchański et al., 2021). Intermediate 3D classification steps of our apo data set provided evidence for at least two distinct conformations (Fig. SI1), consistent with our biochemical assays that suggest a mixture of states. In the main reconstruction, loop C is uncapped over an empty agonist binding site and the hydrophobic gate at the L9' position is closed.

In a second lower-resolution reconstruction accounting for ~30% of the particles, the hydrophobic gate is open, bearing a strong resemblance to both the Carb- and nicotine-bound conformations (see below).

The main reconstruction from the apo dataset led to a structure at 2.9 Å resolution referred to as nAChR$^{apo/resting}$ (Fig. 1). nAChR$^{apo/resting}$ exhibits the typical pLGIC fold, with the five subunits arranged pseudo-symmetrically in an □-□-□-□-□ clockwise fashion about a central ion pathway. Each subunit consists of a short N-terminal □-helix followed by ten □-strands organized into a □-sandwich, four transmembrane □-helices (M1-M4) and a long intracellular MA □-helix between M3 and M4 that extends into the cytoplasm, although it is not completely defined (Fig. SI3: in both this and the agonist-bound reconstructions, densities for the intracellular domain become faint towards the N-terminal end of M4 indicating flexibility or disorder). With its empty neurotransmitter sites and a closed hydrophobic gate, nAChR$^{apo/resting}$ can be confidently assigned to the resting conformation. This apo structure is similar to the recently solved □-bungarotoxin (□BTX)-bound *Torpedo* nAChR structure (Rahman et al., 2020) (C□ RMSD = 1.4 Å, Fig. SI5). Both structures permit modeling features that were not previously resolved in Unwin's pioneering 4 Å resolution nAChR structure (Miyazawa et al., 2003; Unwin, 2005), including bound carbohydrates and lipids, register discrepancies in the transmembrane domain, and C-terminal extensions beyond M4.

The Carb and nicotine data sets led to 3.1 Å and 2.3 Å resolution reconstructions (named nAChR^{carb} and nAChR^{nicotine}) both with bound ligands readily discernible in each of the binding sites located in clefts at the □-□ and □-□ interfaces. In both structures, the C (□9- □10) and F (□8-□9) loops from the principal □ and complementary □/□ subunits, respectively, close around the bound agonist. The ion conducting pathways of nAChR^{carb} and nAChR^{nicotine} adopt an open conformation at the level of the L9' activation gate, thus accounting for the high binding affinity for EthBr. The conformations at -1' are similar to those observed in agonist-bound structures of neuronal nAChRs, conformations that are deemed desensitized (Gharpure et al., 2019; Noviello et al., 2021; Walsh et al., 2018) yet permit ion passage in simulations (see below). Diffuse electron density is also observed in the pore (see below).

Agonist binding to two non-equivalent sites

nAChR^{Carb} defines the modes of agonist binding to the non-equivalent sites located at the interfaces between the □-□ and □-□ subunits (Fig. 2). Although there is contradictory evidence as to which of the two orthosteric sites exhibits higher affinity binding (Andreeva et al., 2006; Nayak and Auerbach, 2013; Prince and Sine, 1996), the extracellular domains of the □-□ and □-□ subunits are virtually superimposable (all atoms RMSD of 0.96 Å), with both agonist sites possessing similar geometries in terms of the first shell of residues interacting with the bound Carb. Residues in the aromatic box, loop B □W149, loop C □Y190/□Y198 and loop D □W55/□W57, wrap tightly around the Carb quaternary amine so that it forms an archetypical cation-□ interaction with □W149 (Xiu et al., 2009; Zhong et al., 1998) and interacts with both the hydroxyl of □Y93 and the backbone carbonyl of □W149 (Fig. 2a). The carbamoyl moiety of Carb is sandwiched between loop C, □C192, □C193 and □Y198, loop B, □T150, and loop E, □L109/□L111 and □L119/□L121. The archetypical interaction between the agonist H-bond acceptor, here the carbonyl of Carb, and a functional group on the receptor, here the backbone carbonyl of □N107/□N109, (Blum et al., 2010) could be mediated through a water molecule, as is the case for nicotine binding to both neuronal (Gharpure et al., 2020) and muscle nAChRs, as well as palonosetron binding to the 5-HT3 receptor (Zarkadas et al., 2020). The carbamoyl nitrogen of Carb forms a H-bond with the hydroxyl of □Y198.

Beyond the first shell of interacting residues, an ensemble of side chain differences distinguish □-□ from □-□. Four sets of residues on the complementary face, □K34/□S36, □E57/□D59, □H172/□I178, and □Y117/□T119, that are primary determinants of the slower agonist dissociation from one of two orthosteric sites (Prince and Sine, 1996; Sine et al., 1990; Zhang et al., 1995) form a line spanning four strands on the complementary side at the top of the binding pocket (Fig. 2c). A network of interactions (H-bonds, salt bridges, etc.) links these residues to each other and to adjacent charged residues, notably □E163/□165 and □D174/□180. While the degree of "capping" at both orthosteric sites is virtually identical (Fig. 2a), the four bulkier side chains at the □-□ site extend towards loop C possibly stabilizing the capped conformation, while weaker interactions at the □-□ site may render the loop more prone to uncap.

The side chain differences between the sites extend down towards □K145, a residue conserved in most □ subunits that forms a complex network of intra- and inter-subunit interactions in the agonist-bound conformation (Fig. 2d). □K145 lies at a distance compatible with both a salt bridge and a cation-□ interaction with □D200 and □Y93, respectively, contacts the aromatic cage front wall □Y190, and forms a backbone hydrogen bond with □N94. □K145 also extends towards loop F forming a salt bridge at the □-□ interface with □D177 (2.3 Å) that is absent at the □-□ interface (the □D177 equivalent is □A183). Loop F □D174 and □H172 are also positioned at the □-□ interface to hydrogen bond with the side chain hydroxyl and backbone NH of □T191 and thus stabilize the capped loop C conformation, while these interactions at the □-□ interface are mediated solely by □D180 (□H172 is replaced by □I178). These latter differences may contribute towards a preferentially closed loop C at the □-□ versus the □-□ site. Mutations of □K145, □D200 or □D174/δD180 influence agonist binding affinity and impair the efficacy of agonist induced gating, primarily by slowing channel opening (Akk et al., 1996; Blum et al., 2011; Mosesso and Dougherty, 2018; Mukhtasimova et al., 2005).

Altogether we pinpoint an ensemble of interactions that are present at □-□, yet absent at □-□. The absence of these interactions at □-□ could lead to faster agonist dissociation due to increased fluctuations between the capped and uncapped conformations of loop C. Note that non-equivalent orthosteric sites have previously been described for neuronal nAChRs. The lower affinity of agonists for the □3□4 compared to the □4□2 nAChR was attributed to a less compact binding pocket (Gharpure et al., 2019), while a triplet of side chain differences on the complementary face explains the lower agonist sensitivity at the □4-□4 interface compared to the □4-□2 interface(Walsh et al., 2018).

Binding of nicotine to muscle versus neuronal nAChRs

Nicotine is a more potent activator of the neuronal □4□2 nAChR than of the muscle (such as *Torpedo*) □1□1□□ nAChR (Fig. 1b), with lower binding affinity protecting muscles from uncontrollable and possibly fatal contractions in response to inhaled nicotine (Grutter et al., 2003; Xiu et al., 2009)). The lower affinity of the muscle nAChR for nicotine occurs despite the conservation of key agonist site residues. A comparison of nAChR$^{\text{nicotine}}$ to the nicotine bound □4□2 nAChR structure (Fig. 3) shows that while the important residues in the aromatic box adopt similar geometries, □Y198 (□4Y204) in nAChR$^{\text{nicotine}}$ twists and translates slightly away from the bound nicotine (~1-1.5 Å difference) and there are subtle differences in the positions of □Y190 (□4Y197) and □W55/□W57 (□2W57). As a consequence, nicotine binds farther from the indole ring of loop B □W149 in nAChR$^{\text{nicotine}}$ than from the equivalent indole ring in the □4□2 nAChR (4.7 Å and 4.2 Å, respectively). The pyrrolidine ring N^{+}-H is also farther from the backbone carbonyl of the loop B tryptophan in nAChR$^{\text{nicotine}}$ (3.6 Å) than in the □4□2 nAChR (3.4 Å), and the geometry of the putative hydrogen bond between the two is less optimal. Both observations are consistent with functional studies suggesting enhanced interactions between nicotine and the loop B tryptophan in the □4□2 nAChR (Xiu et al., 2009).

All our structures feature a hydrogen bond between the backbones of □G153 and □Y198, a hydrogen bond that was previously hypothesized to be present solely in neuronal nAChRs and to be causal to the enhanced affinity for nicotine (Grutter et al., 2003; Xiu et al., 2009). The lower affinity of muscle nAChRs for nicotine could instead arise from the unique sequence and conformation of loop C. Two prolines, □P194 and □P197, impose a convoluted path so that the vicinal cysteines □C192-□C193 are positioned closer to the nicotine pyrrolidine ring, instead of extending further to the complementary subunit, as is the case in the □4□2 nAChR (Fig. 3c). The altered position of □C193 sterically forces □Y198 to translate and twist away from the bound nicotine, increasing the volume of the binding pocket and loosening the ligand packing in the aromatic box. Of note, substitution of the analogous □7P197 with isoleucine in the low-affinity □7 nAChR enhances nicotine binding affinity (Grutter et al., 2003). Furthermore, three residues in loop C of the muscle nAChR (□V188, □Y189, □T191) are replaced by charged residues in the neuronal nAChR (□4R195, □4K196, □4E198), yielding significant differences in the electrostatic environment of the site and permitting an additional intersubunit salt bridge (□4R195-□2D171) that stabilizes the closed C loop conformation. The replacement of loop C residues in the *Torpedo* nAChR with their aligned counterparts in the □4□2 nAChR, however, led to only subtle shifts in potency (both increases and decreases), suggesting that the underlying determinants are more complex (Table SI2).

nAChR-lipid interface

The *Torpedo* nAChR is sensitive to the lipidic composition of the membrane in which it is inserted and requires cholesterol and/or negatively charged lipids to gate (daCosta and Baenziger, 2009). We observed electron density at the periphery of the TMD that could correspond to bound lipids. Nine/six/eleven regions of density were modeled as 1-palmitoyl-2-oleoyl phosphatidylcholine (POPC) in nAChR$^{\text{apo/resting}}$/nAChR$^{\text{Carb}}$/nAChR$^{\text{nicotine}}$ (increasing numbers of lipids are modeled in reconstructions with increasing resolution). The bound lipids are typically found at one of two types of sites: an inner leaflet site (Fig. 4) framed mostly by M3 from the principal subunit and M1 and M4 from the complementary subunit; and an outer leaflet site typically bordered by M4, M3 and the M2-M3 loop from one subunit and M1 from the adjacent subunit. Even though the lipids bound to each of these two types of sites adopt similar binding poses, there are variations in the positions of the choline headgroup that likely arise due to the absence of specific coordinating interactions. The lack of coordinating residues suggests that the binding sites may accommodate different lipid head groups, a structural observation consistent with the low specificity of the *Torpedo* nAChR for neutral and anionic lipids (daCosta et al., 2009; Thompson and Baenziger, 2020).

One lipid is observed at each of the 5 inner leaflet sites in nAChR$^{\text{nicotine}}$ (4 and 3 are defined in the lower resolution nAChR$^{\text{aoo/resting}}$ and nAChR$^{\text{Carb}}$, respectively). In each case, the lipid phosphate is loosely bound between two positively charged residues (e.g. □R301 and □K449 at the □-□ site; Fig 4a), with the principal site cationic side chain (e.g. □R301) held in place by a stacking interaction with both an M4 tryptophan (e.g. □W399) and an M3—MX linker histidine (e.g. □H306)

An aromatic side chain (e.g. □F242) also forms a stacking interaction with one acyl chain. These 5 residues, widely conserved among nAChR subunits and those from other species, constitute a signature motif that could shape a general phospholipid binding site that has a higher affinity for anionic lipids. Interestingly, the MD simulations (see below) show that a lipid, either POPC or POPA, binds quickly to each of the 5 inner leaflet sites and remains bound throughout the simulations. The inner leaflet site is connected directly to the intracellular mouth of the pore by a salt bridge between M4 (e.g. □D407) and the back of M2 (e.g. □K242), which exists in the vast majority of pLGICs of known structure. Disruption of the salt bridge, in the □ and □ subunits, was recently shown to alter channel gating (Strikwerda and Sine, 2021). Steroids have been observed bound to this site in the anionic □1 and □5 GABA$_{A}$R (Laverty et al., 2017; Miller et al., 2017), and lipid binding to this site in ELIC slows the rates of desensitization (Hénault et al., 2019).

Altogether, this site emerges as a potential hotspot for lipid modulation for the entire pLGIC superfamily. Exploring its properties will require comprehensive functional studies. Here, the semi-conserved residues within or next to this pocket were individually mutated to Ala and the effects of these mutations assessed using two-electrode voltage-clamp electrophysiology (Table SI3). Four of the seven mutants (□Y234A, □R301A, □H306A, and □H408A) expressed robustly and influenced the EC50 for ACh by <2-fold relative to WT, despite directly interacting with intracellular leaflet lipids. On the other hand, oocytes injected with the remaining three mutants, □K242A, □W399A, and □D407A did not produce ACh-induced current. At the conserved M2-M4 salt bridge formed between □K242 and □W399, non-conservative mutations were previously shown to abolish function in several pLGICs (Cymes and Grosman, 2011; Mesoy et al., 2019). Put together, this Ala-scan of one lipid site merely indicates: i. that the disruption of one side chain in one lipid interaction site is not enough to abolish function, and ii. that future studies are needed to understand how the lipid site communicates with close-by positions intolerant to mutations.

Although there is no conserved motif that interacts with the lipids in the outer leaflet, both a positively charged residue on M3 (e.g. □K276) and the M2-M3 loop from the ECD form a shallow cavity for the headgroup (Fig. SI7). A set of hydrophobic side chains also forms van der Waals interactions with the acyl chains (mostly on the side of M4). Significantly, M4 from □□, and to a lesser extent from □□, tilt away from the rest of the TMD upon agonist binding, with the outward tilt leading to a repositioning of the adjacent outer leaflet lipids. In □□, the lipid enters the void between the end of M4 and the rest of the TMD where it contacts the strictly conserved Cys-loop FPF motif, while in □□, the glycerol backbone of the lipid wedging between the side chains projecting out from M3 and M4. The dynamic nature of M4 is further supported by the observation of ill-defined 'ghost' densities in nAChR^{nicotine}, likely due to a small fraction of particles with "attached" □M4s. Dynamic movements of M4 may underlie both the uncoupling of binding and gating that occurs with the *Torpedo* nAChR in membranes lacking cholesterol/anionic lipids and the lipid-dependent effects on the rates of desensitization in ELIC (daCosta and Baenziger, 2009; daCosta et al., 2013; Hénault et al., 2019).

The peripheral M4 □-helix in the TMD of each subunit contributes a large fraction of the lipid-exposed surface. The C-terminus of each M4 (post-M4) extends towards the apex of the receptor with increasing lengths in the □, □, □ and □ subunits. In □, □ and □, post-M4 interacts extensively with the ECD, including with the carbohydrate chains covalently linked to □N142, □N141 and □N143, respectively. Although it has been hypothesized that post-M4 - ECD interactions impact channel function to facilitate lipid sensing, we show here that C-terminal deletions have little effect on the agonist-induced response (Fig. SI6). On the other hand, M4 is obligatory for the functional expression of most pLGICs (Haeger et al., 2010; Thompson et al., 2020), with the notable exception of the prokaryotic homolog, ELIC (Hénault et al., 2019).

Conformational changes in the pore: an upper activation gate and a lower constriction

The pore of every pLGIC is encircled by the M2 □-helices from each subunit, with side chains extending into the pore lumen (Wilson and Karlin, 2001; Wiltfong and Jansen, 2009). Functional studies along with the available structural data locate the activation gate in the upper region of the pore where hydrophobic side chains in four concentric rings at the 9', 13', 16' and 17' positions project into the pore (Fig. 5). In the apo conformation, the activation gate is constricted (2-3 Å radius) leading to a >10 Å long narrow hydrophobic microenvironment. Molecular dynamics simulations feature dewetting of this hydrophobic microenvironment (data not shown), impeding ion conduction, in agreement with simulations carried out on many closed-pore pLGICs (Aryal et al., 2015; Kumar et al., 2020; Polovinkin et al., 2018).

In the nAChR^{carb} and nAChR^{nicotine}, the M2 □-helices tilt and twist away from the pore so that side chains, originally protruding into the lumen, project towards the adjacent M2 □-helices. A striking example is □F16' (□F267), which tip moves ~7 Å away from the pore axis. The movements of the M2 □-helices are asymmetrical, with □ subunits moving more (average of 2.35 Å at the level of 9' Ca) than □, □ (1.9 Å) and □ (1.7 Å). These motions lead to a significant increase in pore radius, enough to permit wetting of the pore and access of ions in simulations restrained to the experimental conformations. Different pLGIC structures with open activation gates display a range of pore diameters reflecting a diversity of hydrophobic side chains that project into the pore lumen and different amplitudes of M2 outward motions. Notwithstanding this variability, wetting/dewetting is a conserved feature of pore activation gates (Rao et al., 2021).

The lower region of the pore features a constriction at the level of residues -1' and 0' (~2 Å in radius), reminiscent of the constrictions found in agonist-bound structures of neuronal nAChRs (Fig. SI8). Although it is tempting to define this constriction to a closed desensitization gate, cryo-EM density maps are not unambiguous in the positional assignment of anionic side chains. In nAChR^{carb}/nAChR^{nicotine}, these acidic side chains are best modeled in conformations pointing away from the pore. Switching rotamers would significantly change the diameter of the constriction. Given the ambiguity in the positions of these side chains, we are cautious about interpreting the conformation of the agonist-bound nAChR structures.

To better assess the conformation of the pore, we performed a series of 500 ns long simulations of the agonist-bound state of the nAChR embedded in a fully hydrated lipid bilayer. When the structure is restrained to the conformation observed experimentally, we systematically observe the full hydration of the pore, confirming that the hydrophobic gate (L9') is open (Fig. 5f,g). There is also a continuous hydration of the lower pore and the stochastic presence of cations. Such a wetting is also apparent in reported simulations of the agonist-bound □3□4 nAChR structure deemed desensitized (Gharpure et al., 2019). The -1' acidic residues flip in and out of the pore, albeit spending a larger fraction of time in the outward configuration. In contrast, when the restraints are removed, the pore shrinks and reaches a conformation where the upper hydrophobic gate is dewetted, typically within ten nanoseconds. Yet the lower region of the pore remains open (Fig. 5f,g). A similar pore closure has been observed in MD simulations of the agonist-bound □4□2 nAChR (Oliveira et al., 2019).

Missing elements can cause simulated systems to drift away from an experimental structure. In the nAChR^{Carb} and nAChR^{nicotine} maps, diffuse electron density is present in the pore between 6' and 20'. We modeled three POPC molecules, one head-down and two head-up, to account for those densities. In simulations with lipids in the pore, the pore remains fully stable in a conformation akin to nAChR^{carb}/nAChR^{nicotine}, but with the upper activation gate essentially filled with the hydrophobic tails of the bound POPC (Fig. 5g, SI9). The dynamics of the bound lipids are in qualitative agreement with the experimentally observed diffuse electron densities (Fig. 5d,e). The binding of lipids to the pore is not surprising given that the alternating apolar/polar chemical nature of the pore is a good environment for amphipathic molecules. Some nanodiscs may be destroyed during the concentration step just prior to sample deposition on the cryoEM grids thus releasing lipid that then binds to the pore (indirect evidence for this is the occasional presence of liposomes in the cryoEM images). Six detergent molecules in the pore are observed in crystal structures of the nAChR homolog, GLIC (Bocquet et al., 2009). Inspection of the agonist-bound □4□2 and □3□4 neuronal nAChR reconstructions also reveals the presence of diffuse densities within the pore (Fig. SI10). In fact, lipids are observed bound to the pores of several ion channels, such as the bacterial mechanosensitive channel, MscS (Reddy et al., 2019).

One possible interpretation of our structures, buttressed by the MD simulations, is that the transient formation of the open state allows lipids to lodge in the pore to block closing of the desensitization gate ultimately leading to the formation of a transient state along the reaction coordinate between the open and desensitized conformations. Alternatively, the lipid bound to the pore may stabilize an agonist-induced pre-open state where the ECD and upper activation gate are open, but the lower desensitization gate has not fully opened. Further experimental work is required to identify the gate that blocks ion flux in the desensitized state and thus to fully define desensitization of the muscle nAChR

Conformational changes associated with agonist binding

The conformational changes that define pLGIC function are often viewed through one of two lenses: either globally with an emphasis on quaternary re-arrangements or sequentially starting from the binding site and then moving progressively down to the pore. These two lenses approximate allosteric versus induced fit models of the conformational transitions. We first focus on the latter lens, starting with the two orthosteric sites, the ECD/TMD interface and the pore. We then describe the global quaternary re-arrangements in the context of the activation mechanisms of other pLGICs.

Increased agonist affinity drives conformational transitions from the resting state to the open and desensitized states. The K_d values for Carb (ACh) evolve from 30 µM (800 nM) to 25 nM (2 nM) in the transition from the resting to the desensitized state (Boyd and Cohen, 1980). The closing of loop C around the bound agonist is a major driver of this increased agonist affinity (Fig. 5e, Movie SI1). The $C_{□}$ carbons of the vicinal cysteines at the apex of loop C, □C192 and □C193, translate ~7-9 Å towards the bound Carb, which reduces the volume of the agonist pocket. The movement of loop C, along with subtle movements of loops A, E, D and B (in order of decreasing amplitude), re-position the aromatic box residues, □W149, □Y190, □Y198 and □W55/□W57 tightly around the quaternary amine of Carb likely leading to the enhanced affinity. The closing of loop F from the □/□ subunits to interact with loop C from the □ subunit also contributes to the stability of the high affinity state by locking the capped loop C conformation.

The movement of loops C and F at both orthosteric sites occurs concomitantly with that of the α and γ/δ subunits towards each other (Fig. 6a-c, Movie SI1) causing a ~5-10% increase in the buried surface area at the α-γ and α-δ interfaces alongside a decrease in the buried surface areas at non-agonist binding interfaces. More specifically, closure of loop C (the $\beta 9$-$\beta 10$ loop) occurs with a downward rocking and twisting motion of the adjacent regions of the $\beta 9$ and $\beta 10$ strands towards the bound agonist and complementary γ/δ subunit, while the distal membrane-juxtaposed regions of the $\beta 9$ and $\beta 10$ strands pivot in the opposite direction up and towards the adjacent β/γ subunits (Fig. 6f red arrows) The motions of $\beta 9/\beta 10$ extend to the adjacent β-sheets through a network of non-covalent interactions resulting essentially in a rigid-body movement of the ECD. The relative motion of the the α and γ/δ subunits also drives $\beta 1$-$\beta 2$ loop, Cys-loop and $\beta 10$-M1 linker of the $\alpha_\gamma/\alpha_\delta$ subunits closer to the adjacent β/γ subunits, which ultimately causes the N terminus of αM1 to tilt towards β/γ.

Loop F on the complementary face, rocks up and in towards the bound agonist while the distal membrane juxtaposed region of loop F (i.e. the $\beta 8$-$\beta 9$ loop) pivots outward from the pore, a motion that extends to the remainder of both the γ and δ subunits (Fig. 6f blue arrows). The concerted motions of the $\beta 8$-$\beta 9$ loop and $\beta 10$-M1 linker create a 2-3 Å widening below the neurotransmitter site between the α and γ/δ subunits. Significantly, the $\beta 8$-$\beta 9$ loop and $\beta 10$-M1 linker on γ/δ engage tightly with the adjacent αM2-αM3 linker. The outward rocking motions of the $\beta 8$-$\beta 9$ loop and $\beta 10$-M1 couple directly with movements of the αM2-αM3 linker so that αM2 and αM3 twist out and away from the pore (Fig. 6f violet arrow and Movie SI3). A role for the $\beta 8$-$\beta 9$ loop in agonist-induced conformational transition is supported by functional studies (Gleitsman et al., 2008; Shen et al., 2018; Sine et al., 2002) although a central role in gating has not been fully appreciated. Interestingly, a rate-equilibrium free energy relationship analysis suggests that the motions of the $\beta 8$-$\beta 9$ loop occur earlier in the gating process than the motions of other structures at the ECD-TMD interface (Jha et al., 2012). The movements of the $\beta 8$-$\beta 9$ loop and $\beta 10$-M1 linker may be required to facilitate the tilting of M1 leading to a fully activated state.

Muted movements of loop C and F at the non-agonist binding interfaces attenuate the tertiary deformations in the ECD of each non-α subunit. Although the $\beta 8$-$\beta 9$ loop and $\beta 10$-M1 linker on the complementary side of each non-agonist-binding interface still engage tightly with the adjacent M2-M3 linker on the principal side, the positions of these motifs remain relatively unchanged upon agonist binding. As a result, the asymmetric motions at both binding and non-binding interfaces couple together so that the cores of α_{γ}-β-δ and α_{δ}-γ move essentially as rigid bodies in opposite directions (Fig. 6d, Movie SI2). The net effect of these rigid body motions is that there is less of a twisting motion in the ECDs of the β, γ and δ subunits. Instead, γ/δ, and to a lesser extent β, simply follow the movements of loop F, with their membrane juxtaposed regions rocking outwards from the pore translating into similar rigid body-like outward rocking/tilting motions of the four TMD α-helices in the β, γ and δ subunits.

Comparative Gating Mechanism

The presented structures define an allosteric mechanism whereby structural rearrangements around the two neurotransmitter sites couple with opening of the activation gate. Rocking motions of the ECDs of the principal $□_{□}/□_{□}$ and complementary □/□ subunits towards each other are associated with both a tightening of the agonist sites and scissor-like motions of the □ subunit interfacial elements - the □1-□2 loop, Cys-loop and □10-M1 linker move in one direction while M2 and M3 move in the opposite direction in concert with □8-□9 loop and □10-M1 linker from the complementary subunit (Fig. 6f, Movie SI3,SI4). Smaller rearrangements at non-agonist binding interfaces cause $□_{□}$-□-□ and $□_{□}$-□ to move essentially as two separate blocks (Fig. 6d, Movie SI2). Collectively, these tertiary and quaternary deformations lead to an outward flexing at each ECD/TMD interface that couples with an outward tilting and twisting of each pore lining M2 □-helix to permit cation flux.

The activation mechanism of the muscle-type nAChR overlaps with that seen recently in the human □7 nAChR (Movie SI5a). In both cases, agonist binding correlates with motions of principal and complementary faces around the orthosteric sites, although in the □7 nAChR the closure of loop F is absent. In fact, the closing of the principal and complementary faces around the orthosteric sites are conserved in the entire pLGIC family, with similar motions occurring in the homomeric mouse serotonin 5-HT_3 receptor, the heteromeric human □1□3□2L $GABA_A$ receptor and the zebrafish □1 glycine receptor (Movie SI5a). Larger rocking motions at the apex of the principal subunit ECD, however, are observed in both anionic receptors.

In the TMDs, the outward blooming motions observed in our apo (closed) to agonist-bound transition mimic those observed in the toxin-bound (closed) to epibatidine-bound (deemed desensitized) □7 nAChR transition, albeit motions in the *Torpedo* nAChR are less symmetrical (Movie SI6). On the other hand, our agonist bound structures lack the strong tilt of the transmembrane □-helices and wider pore opening seen in the agonist-bound □7 nAChR structure solved in the presence of epibatidine and the positive allosteric modulator, PNU-120596. The activation mechanism observed here differs from the gating mechanism from pioneering time-resolved cryoEM imaging (Unwin, 2013; Unwin and Fujiyoshi, 2012), where the $□_{□}$ subunit motion was transmitted to the □ subunit, with the ECD and TMD of □ both tilting outward from the pore while flexing at the ECD/TMD interface. The discrepancy may be due to a possible error in register in the lower resolution structure leading to an incorrect assignment of □ to □ (Rahman et al., 2020).

Finally, a parallel can be drawn between the muscle-type nAChR and the □1□3□2L $GABA_A$ receptor, which both feature two agonist binding sites. Upon agonist binding, the subunits in both move as 'blocks', which are delineated by the two agonist-binding interfaces (Movie SI7).

Conclusions

The apo and agonist bound structures reported here reveal the mechanism that underlies activation of the channel pore of a heteromeric muscle-type nAChR and highlight a previously unappreciated involvement of the complementary subunit in the gating process. The structures provide a precise, multi-state, structural template for interpreting the vast catalogue of structure-function relationships derived from decades of biochemical and mutagenesis studies on the *Torpedo* nAChR. They also elucidate the structural basis for both agonist binding affinity and lipid binding to this lipid-dependent pLGIC. Our work contributes to a central debate in pLGIC structural biology, how to correlate solved structures with physiological states, by applying a biochemical assay to define the conformational landscape of our cryo-EM samples and by showing that our nanodisc reconstituted nAChR retains the ability to undergo agonist-induced conformational transitions. We provide several lines of evidence that question the direct correlation of agonist-bound structures to the electrophysiologically defined desensitized state. This uncertainty may extend to other agonist-bound nAChR structures. Further studies are required to define the mechanism by which ion flux is blocked in the desensitized state.

Acknowledgements

The work was funded by ERC Starting grant 637733 Pentabrain and grant number 113312 from the Natural Sciences and Engineering Research Council of Canada. JB's sabbatical stay was partly funded by the University Grenoble Alpes. It used the platforms of the Grenoble Instruct-ERIC center (ISBG ; UMS 3518 CNRS-CEA-UGA-EMBL) within the Grenoble Partnership for Structural Biology (PSB), supported by FRISBI (ANR-10-INBS-05-02) and GRAL, financed within the University Grenoble Alpes graduate school (Ecoles Universitaires de Recherche) CBH-EUR-GS (ANR-17-EURE-0003). The electron microscopy facility is supported by the Rho□ne-Alpes Region, the FRM, the FEDER and the GIS-IBISA. F.D. acknowledge the State-Region Grand-Est Plan "Technological Innovations, Modeling and Personalized Medical Support" (IT2MP) and the European Regional Development Funds (ERDF) for generous support. We thank Instruct-ERIC, part of the European Strategy Forum on Research Infrastructures (ESFRI), Instruct-ULTRA (EU H2020 grant no. 731005) and the Research Foundation Flanders (FWO) for support with megabody discovery.

Author contribution

Conceptualization, E.Z., H.N and J.B; Methodology, and Investigation, all authors; Writing – Original Draft, J.B and H.N.; Writing – Review & Editing, all authors; Funding Acquisition, J.B, F.D., H.N.; Methodology and Resources, T.U., J.S. and G.S.; Supervision, H.N. and J.B

Figure Legends

Figure 1. Structures of the *Torpedo* nAChR. a. Fluorescence (AU: arbitrary units) of EthBr alone in solution (grey) or in the presence of nAChR reconstituted in liposomes or in nanodiscs (black). Arrows indicate the addition of Carb (black), triggering the agonist-induced conformational change, and dibucaine (grey) displacing EthBr from its nAChR pore binding site. **b.** The curves represent a fit using the Hill equation to the normalized current responses of the *Torpedo* nAChR in the presence of increasing concentrations of acetylcholine (black), Carb (blue) and nicotine (red). Circles represent averaged data with standard deviations (n = 8, 10 and 9, respectively). The inset shows a prolonged 10 minute whole cell response to 100 □M acetylcholine (ACh). **c.** Top and side views of the main apo nAChR cryo-EM reconstruction (nAChR$^{apo/resting}$) colored by subunit, with the nanodisc density represented as a transparent white surface (left). Cartoon representation with glycans as sticks (right). **d-e.** Side and top views of the cryo-EM reconstructions for nAChR^{Carb} and nAChR^{nicotine}. The agonist formula and electron density around one agonist are shown. This subunit color code is maintained throughout the report with the apo- and agonist-bound structures in vivid and pastel colors, respectively.

Figure 2. The non-equivalent □-□ and □-□ sites. a. Top and side views of the □-□ and □-□ sites with bound Carb. Residues close to the bound agonist (ball-and-sticks) are represented as sticks. **b.** Top view of a slab of the nAChR^{Carb} reconstruction. The Carb molecule is colored in red, at the □/□ and □/□ sites (noted as plain or dashed rectangles). **c.** Top views of the □/□ and □/□ sites highlighting the complementary subunit residues that differ in □ verus □ **d.** Views of the □/□ and □/□ sites showing the interactions between loops C and F, together with interactions at the principal subunit residue K145.

Figure 3. Nicotine binding to the muscle-type nAChR^{nicotine} versus the neuronal □4□2 nAChR. a. and b. Top down and side views, respectively, of the binding site of nAChR^{nicotine} (□-□, grey or color coded loop B: green; loop C: yellow; loop D: violet; loop E: pale purple). Nicotine and side chains within 5 Å of the bound nicotine are shown as cyan ball-and-sticks and sticks, respectively. Nicotine and analogous side chains in the □4□2 nAChR are overlaid as pink sticks. In B, loop C is removed for clarity. The principal □ subunits were used for superimposition. **c.** Overlay of the binding loops of nAChR^{nicotine} and the nicotine-bound □4□2 nAChR (same color code) with an emphasis on the G153/K160 position (red sphere for nAChR^{nicotine}, pink sticks for the □4□2 nAChR). The distances between equivalent C□s are indicated for 3 loop C residues.

Figure 4. Lipid sites. a,d. Overview of the lipids bound to nAChR^{nicotine} . The TMD is represented as a cartoon (same orientation and colors as in Fig. 1) while the lipids appear as pink (outer leaflet) or white (inner leaflet) sticks. **b,e.** Close-up views of the inner leaflet lipid bound at the □/□ interface. The lipid is depicted as white sticks, the conserved residues that build its site are shown as sticks (red: negatively charged, blue: positively charged, purple: aromatic). **c.** Sequence alignment of the conserved residues building the inner leaflet lipid site.

Figure 5. Conformations and wetting of the pore. a. Side views of the M2 helices of nAChR^{apo} (the two foreground helices are removed) with pore facing residues as spheres (yellow hydrophobic, green polar, blue negatively charged). The pathway accessible to ions and water molecules (calculated by CHAP) is indicated by a black outline. **b.** Overlay of the accessible pathways in nAChR^{apo} (blue) and nAChR^{carb} (green). Approximate diameters at constrictions are noted. **c.** Side views of the M2 helices of nAChR^{carb}, with orthogonal views of two slabs at the level of the activation gate and of the lower pore constriction. **d.** Side view of the nAChR^{carb} map (the density around the two foreground subunits is removed) with the diffuse density inside the pore in grey **e.** Snapshot of the M2 helices, taken during a MD simulation run of nAChR^{carb} featuring 3 POPC molecules in the pore. The average density for the POPC molecules is shown. **f.** Side view of the M2 helices, taken during a MD simulation run of nAChR^{carb}, at 50 ns where restraints to the experimental structures are still applied (left) and at 600 ns after relaxation (right). Water molecules are depicted as spheres. **g.** Water, sodium ions and POPC density profiles along the channel axis, during an MD simulation run of nAChR^{carb} by itself (top, the dashed line indicates the release of restraints on the pore) and when 3 POPC molecules are added in the pore (bottom). The y axis is indicated on panel a. Asterisks indicate the positions of the snapshots of panel f.

Figure 6. ECD transition, gating mechanism. a and c. Overlay of the □$_{□}$ principal subunits, from two opposite points of views, in the resting (grey) and nicotine-bound conformations. Both overlays are after superimposition of the complementary □ subunits. **b.** Cartoon representation of the □/□ ECDs, color-coded and radius-coded by RMSD between nAChR$^{apo/resting}$ and nAChR^{nicotine}. **d.** Top view of the ECD pentamers as cartoons, showing how ECDs moves as two □$_{□}$-□-□ and □$_{□}$-□ blocks separated by binding interfaces. The arrow indicates the subunit used for superimposition. **e.** Close-up view of the orthosteric binding site, highlighting the large motions of loops C and F. Those loops of nAChR$^{apo/resting}$ are depicted as cartoon (color-coded and radius-coded by RMSD) and overlaid with both □/□ and □/□ from nAChR^{nicotine} depicted as cartoon and sticks. **f.** Schematic of the transition, showing the principal motions coupled with agonist binding.

STAR Methods

Resource availability

Lead Contact

Further information and requests for resources and reagents should be directed to and will be fulfilled by the lead contact, John Baenziger (john.baenziger@uottawa.ca).

Materials Availability

This study did not generate any new unique reagents.

Data and code availability

- The cryo-EM electron density maps and atomic model coordinates have been deposited in the EMDB and RCSB, respectively, under the following accession codes (Table SI1): EMD-14048 / PDB ID 7QKO for the apo-resting conformation, EMD-14064 / PDB ID 7QL5 for the nicotine-bound conformation and EMD-14065 / PDB ID 7QL6 for the carbamylcholine-bound conformation.

- No original code was generated in this study.

- Any additional information required to reanalyze the data reported in this paper is available from the Lead Contact upon request.

Experimental Model and Subject Details

- The nAChR was purified from the electroplax tissue (Aquatic Research Consultants, CA) obtained from wild Pacific electric ray *Tetronarce californica* (NCBI: txid7787).

Methods Details

Protein purification and reconstitution in lipid discs

The nAChR was purified on a bromoacetylcholine bromide (BAC)-derivatized Affi-Gel 102 column (Bio-Rad) as previously described (daCosta and Baenziger. JBC 2009), albeit with several modifications. Crude membranes were solubilized 1.5 hours in 1% of sodium cholate Tris Dialysis buffer (TDB: 100 mM NaCl, 10 mM Tris base, 1 mM EDTA, 0.02% NaN_3, pH 7.8) and homemade protease inhibitors cocktail. After ultracentrifugation (140'000 g for 30 minutes) to remove insoluble material, the supernatant was applied by gravity to the BAC affinity column and washed with seven column volumes of TDB supplemented with 1% sodium cholate and 1.05 mM soybean asolectin lipids (Sigma). The bound protein was eluted in 60 mL of the same buffer with, instead, 250 mM NaCl and supplemented with 25 mM Carb (Sigma).

For reconstitution into asolectin liposomes, the eluate was transferred to dialysis bags (10 kDa cut-off) and dialyzed five times against 2 liters of TDB, with buffer change every 12 h. The reconstituted membranes were centrifuged at 120'000 g for 2 h and resuspended in TDB. Protein concentration was determined by BCA assay (Pierce). For reconstitution into lipidic nanodiscs, the affinity purified nAChR was concentrated using a centrifugal filter device with a 100 kDa cut-off (Amicon) to 4 mg/mL and further purified by size-exclusion chromatography on a Superose6 Increase column (GE healthcare) equilibrated with TDB supplemented with 1% sodium cholate and 1.05 mM soybean asolectin lipids. The nAChR elutes in two peaks corresponding to monomeric pentamers and dimeric pentamers linked by a disulfide bond between Cys residues at the C-termini of the delta subunit. Incubation with 15 mM DTT for 1h prior to size-exclusion chromatography leads to predominantly the monomeric form (Fig. SI1). The isolated nAChR was concentrated to 2 mg/mL, incubated for 30 minutes with MSP2N2 (Addgene plasmid # 29520 (Grinkova et al., 2010)) at a 1:5 mol:mol ratio of nAChR to MSP2N2, and then mixed with Bio-Beads (BioRad) added to a final concentration of 400 mg/mL. The following day, the Bio-Beads were settled down by centrifugation (250 g, 5 min) and the supernatant was subjected to size-exclusion chromatography in a Superose6 increase column equilibrated in TBS buffer (25 mM Tris-HCl, 125 mM NaCl, pH 7.5). The fractions containing the monomeric form of the nAChR in reconstituted asolectin-MSP2N2 lipidic nanodiscs (Fig. SI1) were pooled, concentrated to 0.65 mg/mL, aliquoted, snap frozen in liquid nitrogen and stored at -80°C.

Two electrode voltage clamp electrophysiology

Mutants were created from WT *Torpedo* □1, □1, □ and □ nAChR sequences in the pcDNA3 vector using QuikChangeTM site-directed mutagenesis kits (Agilent) and verified by sequencing. The resulting vectors were linearized and capped cRNA produced by *in vitro* transcription using the mMESSAGE mMACHINE® T7 kit (Ambion). Stage V–VI oocytes from *Xenopus laevis* were injected with 5 ng of WT or mutated a1 subunit cRNA along with 2.5 ng each of β1, δ, and γ subunit cRNA and allowed to incubate for 2 to 4 days at 16 °C in ND96+ buffer (5 mM HEPES, 96mM NaCl, 2 mM KCl, 1 mM MgCl2, 1 mM CaCl2, 2 mM pyruvate). Whole-cell currents were measured in response to agonist concentration jumps (flow rate of 5-10 mL/min.) using a two- electrode voltage clamp apparatus (OC-725C oocyte clamp; Holliston, MA) in the presence of 1 mM atropine to prevent the activation of endogenous calcium-activated chloride channels via muscarinic acetylcholine receptors. Whole-cell currents were recorded in HEPES buffer (96 mM NaCl, 2 mM KCl, 1.8 mM BaCl2,1 mM MgCl2, and 10 mM HEPES, pH 7.3), with the transmembrane voltage clamped at -60 mV. When assessing the potency of nicotinic agonists, a transmembrane potential of +60 mV was applied to minimize the effects of channel block at high agonist concentrations. Dose responses were acquired from at least two different batches of oocytes. Each individual dose response was fitted with a variable-slope sigmoidal dose-response curve. Plots were created using GraphPad Prism, where each individual dose response was normalized. In the presented dose-response curves, data points were averaged, and curve fits of the averaged data are presented with the error bars representing the standard errors.

Electron microscopy and image analysis

The monomeric form of the nAChR in asolectin-MSP2N2 nanodiscs was mixed with the megabody Mb_{NbF3}^{c7HopQ} (Uchański et al., 2021) at a molar ratio 1:3. This megabody binds to the MSP2N2 scaffolding protein, not to the nAChR, and is present to help the nanodisc adopt multiple orientations on the cryo-EM grids. For the Carb and nicotine datasets 500 µM of carbamylcholine or 10 mM of nicotine, respectively, were also added to the mixture. After incubating for 30 minutes on ice, 3.5 µl of each sample were deposited onto glow-discharged (30 mA, 50 s) Quantifoil Au/C R 1.2/1.3 grids, blotted for 6 s with force 0, at 8°C and 100% humidity using a Mark IV Vitrobot (FEI, Thermo Fisher Scientific) and plunge-frozen in liquid ethane for sample vitrification.

The apo and Carb datasets were recorded on a Glacios electron microscope at the IBS (Table SI1, Fig. SI1, SI2), at a nominal magnification of 36'000, and movies (40 frames for the Carb and 60 frames for the apo datasets) were acquired with SerialEM on a Gatan K2 Summit camera. The nicotine dataset was recorded on a Titan Krios electron microscope at the ESRF (Kandiah et al., 2019) (Table SI1, Fig. SI2), at a nominal magnification of 165'000 and movies (60 frames) were acquired with EPU on a Gatan K2 Summit camera mounted after an energy filter 20eV slit width.

For the apo and Carb datasets, the raw movies were imported to Cryosparc (Punjani et al., 2017), aligned and summed excluding the first frame and the CTF estimation was calculated for the non dose-weighted sums. For the nicotine dataset, the raw movies were aligned and summed with MotionCor2 (Zheng et al., 2017) including all frames, the dose-weighted micrographs were imported to Cryosparc, where the CTF estimation was calculated. Particles were autopicked with crYOLO 1.7.6 (Wagner et al., 2019) using the general model for low-pass filtered images and particle coordinates were imported to Cryosparc, where all subsequent steps were performed. Raw particle stacks were extracted at 256 pixels box size for the apo and Carb datasets and at 352 pixels for the nicotine dataset.

The workflow followed from this step was similar for all datasets (Fig. SI1, SI2). Two rounds of 2D classifications were performed and particles from all classes showing clear pLGIC features and the monomeric form of nAChR were selected and submitted to *ab initio* reconstruction & heterogeneous refinement with 3 classes. Although we initially thought that external subunit-specific binders would be required for refinement algorithms to correctly discriminate between the homologous subunits (Laverty et al., 2019; Walsh et al., 2018), initial 3D reconstructions showed that intrinsic structural differences, such as the locations of glycosylation sites and the lengths of the C-termini, were sufficient for subunit assignment. The one class showing the best nAChR features, map integrity and more isotropic viewing angles distribution was selected and refined with Non-Uniform & local refinements (Punjani et al., 2020). The resulting reconstruction was subjected to 3D variability analysis (Punjani and Fleet, 2021) and the resulting clusters were grouped excluding those with poor density quality at the TMD level. Selected particles were refined once more with Non-Uniform & local refinements resulting in the final reconstruction. For the apo dataset, the 3D variability analysis revealed two distinct major conformations, one with closed and one with open hydrophobic gate. Thus, depending on the pore conformation, the clusters were spliced into groups and treated separately; particles from three clusters with closed hydrophobic gate were grouped and refined to the resting conformation and particles from two clusters with open hydrophobic gate were grouped and refined to the open conformation, while a sixth cluster showed poor density at the TMD level and its particles were excluded from further analysis. The open conformation of the apo dataset, though apparently unliganded, showed extended similarity to the carb-bound reconstruction (map correlation of >0.9 in Chimera) and thus was not further analysed.

Model refinement and structure analysis

Existing models were rigidly fitted in the maps. The best match was with the structure of the □3β4 nAChR (6PV7), which was then used to generate an homology model with the SwissModel online service. The sequences were retrieved from the UniProtKB database (The UniProt Consortium, 2017) and the models comprise the residues mentioned below (following the numbering convention of the original model 2BG9). Cycles of real-space refinement in Phenix (Liebschner et al., 2019) were performed, alternating with manual rebuilding in Coot (Emsley et al., 2010) using the maps from Cryosparc and sometimes maps post-processed with DeepEMhancer (Sanchez-Garcia et al., 2021). Validation was performed with Molprobity (Williams et al., 2018) (Table S1). Visual information about the model and its fit in the map are found in Fig. SI3. Figures were prepared with PyMOL (Schrodinger) Chimera (Pettersen et al., 2004) or ChimeraX (Pettersen et al., 2021).

For the nAChR$^{apo/resting}$: A ($\square_{\square}$): 1-331, 370-434, B (□): 1-334, 408-469, C (□): 1-341, 422-500, D ($\square_{\square}$): 1-330, 381-432, E (□): 2-331, 416-489. The model also comprises 14 N-acetylglucosamine (NAG), 19 □-D-mannose (MAN) and 7 □-D-mannose (BMA) residues of N-linked glycosylation attributed to densities protruding from N70, N143 and N208 of □ (C, N141 of β (B) and N141 of the □ subunits (A,D). Elongated density surrounding the TMD were attributed to lipids and modeled as 9 POPC molecules (POV).

For the nAChR^{Carb} : A ($\square_{\square}$): 1-329, 376-425, B (□): 1-336, 405-469, C (□): 1-341, 421-500, D ($\square_{\square}$): 1-322, 376-425, E (□): 2-334, 419-489. One Carb molecule (CCE) was placed at each of the orthosteric sites. The model also comprises 15 N-acetylglucosamine (NAG), 15 □-D-mannose (MAN) and 6 □-D-mannose (BMA) residues of N-linked glycosylation attributed to densities protruding from N70, N143 and N208 of □ (C), N68 of □ (E), N141 of □ (B) and N141 of the □ subunits (A,D).

For the nAChR^{nico} : A ($\square_{\square}$): 1-331, 374-432, B (□): 1-334, 405-469, C (□): 1-340, 419-501, D ($\square_{\square}$): 1-331, 378-425, E (□): 2-335, 418-489. One nicotine (NCT) and one water (HOH) molecule were placed at each of the orthosteric sites. The model also comprises 12 POPC molecules (POV), 15 N-acetylglucosamine (NAG), 16 □-D-mannose (MAN) and 6 □-D-mannose (BMA) residues of N-linked glycosylation attributed to densities protruding from N70, N143 and N208 of □ (C), N68 of □ (E), N141 of □ (B) and N141 of the □ subunits (A,D).

Molecular Dynamics Simulations

All the simulation setups of the agonist-bound state were built against the nAChR^{Carb} cryo-EM structure. The protein complex together with its glycosylation chains and the two bound carbamylcholine agonist was inserted in an heterogeneous lipid membrane composed of 225 palmitoyl-oleyl-phosphatidylcholine (POPC), 74 palmitoyl-oleoyl-phosphatidic acid (POPA) and 74 cholesterol (3:1:1 ratio) using the CHARMM-GUI interface (Jo et al., 2008; Wu et al., 2014). The complex was solvated with 59,970 TIP3P water molecules (Jorgensen et al., 1983) and 150 mM NaCl.

The initial structures involving 2 and 3 POPC in the pore were obtained by positioning manually one POPC with its head group pointing downwards the pore and one or two POPCs with their head groups pointing upwards. Pore-lipids were initially modeled in a straight conformation to avoid steric clashes.

The parameters for carbamylcholine were generated by CHARMM general force field (CGenFF) (Vanommeslaeghe et al., 2009). The glycosylated-protein and the lipids were described by CHARMM36 protein (Best et al., 2012; MacKerell et al., 1998) and lipid (Klauda et al., 2010) force fields, respectively. Hydrogen mass repartition (Hopkins et al., 2015) was used for all drug-receptor complex simulations, allowing for using a time step of 4 fs.

Program NAMD version 2.14 (Phillips et al., 2005) and 3.0 (Phillips et al., 2020) were employed for all the simulations. The temperature and pressure were maintained at 1 atm and 300K by the Langevin piston method (Feller et al., 1995) and the Langevin thermostat, respectively. Long-range electrostatic interactions were evaluated by the particle-mesh Ewald (PME) algorithm (Darden et al., 1993). Integration was performed with a time step of 8 and 4 fs for long- and short-range interactions, respectively, employing the r-RESPA multiple time-stepping algorithm (Tuckerman et al., 1992). The SHAKE/RATTLE (Andersen, 1983; Ryckaert et al., 1977) was used to constrain covalent bonds involving hydrogen atoms to their experimental lengths, and the SETTLE algorithm (Miyamoto and Kollman, 1992) was utilized for water. We performed 3 independent simulations for the agonist-bound conformation starting with a 60 ns pre-equilibration followed by a 90 ns equilibration period with either no restraints or soft-harmonic positional restraints applying only on heavy atoms of either the membrane or the extracellular domains. The 3 runs were finally conducted with no restraints up to 550 ns. For the pore-bound-POPC simulations, we equilibrated the pore lipids for 60 ns with soft-harmonic positional restraints applying on heavy atoms of the protein. The 3 runs were conducted with no restraints up to 550 ns. The VMD program was employed to analyze and render the MD data (Humphrey et al., 1996). Pore profiles were calculated with HOLE (Smart et al., 1996) or CHAP (Trick et al., 2016).

Quantification and statistical analysis

The cryo-EM single particle reconstruction and associated model building were performed as described in the "Electron microscopy and image analysis" and "Model refinement and structure analysis" sections of the Methods Details, using the software packages Relion, cryoSPARC, Phenix and Coot as detailed in the Key Resources Table. The reported resolutions are based on the "gold-standard" FSC 0.143 or 0.5 criterion (Figures SI1, SI2 and Table SI1). The atomic model evaluation was based on Molprobity scores (Williams et al., 2018) and Ramachandran plots. The cryo-EM data collection, refinement and validation statistics are summarised in Table SI1. For the MD simulations, the statistical analyses were carried out within the VMD software as detailed in the "Molecular Dynamics Simulations" section and the Key Resources Table. For the whole cell electrophysiology experiments, the analysis was done using the GraphPad Prism 8 suite. Details of replicates are given in the individual figure legend, where n is the number of cells that the measurements were taken from. All the values are included in the analysis, error bars represent standard error of the mean and bracketed values indicate the 95% confidence interval. No statistical methods were used to predetermine sample size or to determine whether the data met assumptions of the statistical approach. The experiments were not randomized. The investigators were not blinded to allocation during experiments and outcome assessment.

Declaration of interests

The authors declare no competing interests

References

Akk, G., Sine, S., and Auerbach, A. (1996). Binding sites contribute unequally to the gating of mouse nicotinic alpha D200N acetylcholine receptors. J. Physiol. *496 (Pt 1)*, 185–196.

Andersen, H.C. (1983). Rattle: A “velocity” version of the shake algorithm for molecular dynamics calculations. J. Comput. Phys. *52*, 24–34.

Andreeva, I.E., Nirthanan, S., Cohen, J.B., and Pedersen, S.E. (2006). Site specificity of agonist-induced opening and desensitization of the Torpedo californica nicotinic acetylcholine receptor. Biochemistry *45*, 195–204.

Aryal, P., Sansom, M.S.P., and Tucker, S.J. (2015). Hydrophobic gating in ion channels. J. Mol. Biol. *427*, 121–130.

Best, R.B., Zhu, X., Shim, J., Lopes, P.E.M., Mittal, J., Feig, M., and MacKerell, A.D. (2012). Optimization of the Additive CHARMM All-Atom Protein Force Field Targeting Improved Sampling of the Backbone □, ψ and Side-Chain χ1 and χ2 Dihedral Angles. J. Chem. Theory Comput. *8*, 3257–3273.

Blum, A.P., Lester, H.A., and Dougherty, D.A. (2010). Nicotinic pharmacophore: the pyridine N of nicotine and carbonyl of acetylcholine hydrogen bond across a subunit interface to a backbone NH. Proc. Natl. Acad. Sci. U. S. A. *107*, 13206–13211.

Blum, A.P., Gleitsman, K.R., Lester, H.A., and Dougherty, D.A. (2011). Evidence for an extended hydrogen bond network in the binding site of the nicotinic receptor: role of the vicinal disulfide of the alpha1 subunit. J. Biol. Chem. *286*, 32251–32258.

Bocquet, N., Nury, H., Baaden, M., Le Poupon, C., Changeux, J.-P., Delarue, M., and Corringer, P.-J. (2009). X-ray structure of a pentameric ligand-gated ion channel in an apparently open conformation. Nature *457*, 111–114.

Boyd, N.D., and Cohen, J.B. (1980). Kinetics of binding of [3H]acetylcholine and [3H]carbamoylcholine to Torpedo postsynaptic membranes: slow conformational transitions of the cholinergic receptor. Biochemistry *19*, 5344–5353.

Changeux, J.-P. (2012). The nicotinic acetylcholine receptor: the founding father of the pentameric ligand-gated ion channel superfamily. J. Biol. Chem. *287*, 40207–40215.

Cymes, G.D., and Grosman, C. (2011). Tunable pKa values and the basis of opposite charge selectivities in nicotinic-type receptors. Nature *474*, 526–530.

daCosta, C.J.B., and Baenziger, J.E. (2009). A Lipid-dependent Uncoupled Conformation of the Acetylcholine Receptor. J. Biol. Chem. *284*, 17819–17825.

daCosta, C.J.B., Medaglia, S.A., Lavigne, N., Wang, S., Carswell, C.L., and Baenziger, J.E. (2009). Anionic lipids allosterically modulate multiple nicotinic acetylcholine receptor conformational equilibria. J. Biol. Chem. *284*, 33841–33849.

daCosta, C.J.B., Dey, L., Therien, J.P.D., and Baenziger, J.E. (2013). A distinct mechanism for activating uncoupled nicotinic acetylcholine receptors. Nat. Chem. Biol. 9, 701–707.

Darden, T., York, D., and Pedersen, L. (1993). Particle mesh Ewald: An N□log(N) method for Ewald sums in large systems. J. Chem. Phys. *98*, 10089–10092.

Emsley, P., Lohkamp, B., Scott, W.G., and Cowtan, K. (2010). Features and development of Coot. Acta Crystallogr. D Biol. Crystallogr. 66, 486–501.

Feller, S.E., Zhang, Y., Pastor, R.W., and Brooks, B.R. (1995). Constant pressure molecular dynamics simulation: The Langevin piston method. J. Chem. Phys. *103*, 4613–4621.

Gharpure, A., Teng, J., Zhuang, Y., Noviello, C.M., Walsh, R.M., Jr, Cabuco, R., Howard, R.J., Zaveri, N.T., Lindahl, E., and Hibbs, R.E. (2019). Agonist Selectivity and Ion Permeation in the α3β4 Ganglionic Nicotinic Receptor. Neuron.

Gharpure, A., Noviello, C.M., and Hibbs, R.E. (2020). Progress in nicotinic receptor structural biology. Neuropharmacology *171*, 108086.

Gielen, M., and Corringer, P.-J. (2018). The dual-gate model for pentameric ligand-gated ion channels activation and desensitization. J. Physiol. *596*, 1873–1902.

Gleitsman, K.R., Kedrowski, S.M.A., Lester, H.A., and Dougherty, D.A. (2008). An intersubunit hydrogen bond in the nicotinic acetylcholine receptor that contributes to channel gating. J. Biol. Chem. *283*, 35638–35643.

Grinkova, Y.V., Denisov, I.G., and Sligar, S.G. (2010). Engineering extended membrane scaffold proteins for self-assembly of soluble nanoscale lipid bilayers. Protein Eng. Des. Sel. *23*, 843–848.

Grutter, T., Prado de Carvalho, L., Le Novère, N., Corringer, P.J., Edelstein, S., and Changeux, J.-P. (2003). An H-bond between two residues from different loops of the acetylcholine binding site contributes to the activation mechanism of nicotinic receptors. EMBO J. 22, 1990–2003.

Haeger, S., Kuzmin, D., Detro-Dassen, S., Lang, N., Kilb, M., Tsetlin, V., Betz, H., Laube, B., and Schmalzing, G. (2010). An intramembrane aromatic network determines pentameric assembly of Cys-loop receptors. Nat. Struct. Mol. Biol. *17*, 90–98.

Hénault, C.M., Govaerts, C., Spurny, R., Brams, M., Estrada-Mondragon, A., Lynch, J., Bertrand, D., Pardon, E., Evans, G.L., Woods, K., et al. (2019). A lipid site shapes the agonist response of a pentameric ligand-gated ion channel. Nat. Chem. Biol. *15*, 1156–1164.

Herz, J.M., Johnson, D.A., and Taylor, P. (1987). Interaction of noncompetitive inhibitors with the acetylcholine receptor. The site specificity and spectroscopic properties of ethidium binding. J. Biol. Chem. *262*, 7238–7247.

Hopkins, C.W., Le Grand, S., Walker, R.C., and Roitberg, A.E. (2015). Long-Time-Step Molecular Dynamics through Hydrogen Mass Repartitioning. J. Chem. Theory Comput. *11*, 1864–1874.

Humphrey, W., Dalke, A., and Schulten, K. (1996). VMD: visual molecular dynamics. J. Mol. Graph. *14*, 33–38, 27–28.

Jadey, S., and Auerbach, A. (2012). An integrated catch-and-hold mechanism activates nicotinic acetylcholine receptors. J. Gen. Physiol. *140*, 17–28.

Jha, A., Gupta, S., Zucker, S.N., and Auerbach, A. (2012). The energetic consequences of loop 9 gating motions in acetylcholine receptor-channels. J. Physiol. *590*, 119–129.

Jo, S., Kim, T., Iyer, V.G., and Im, W. (2008). CHARMM-GUI: a web-based graphical user interface for CHARMM. J. Comput. Chem. *29*, 1859–1865.

Jorgensen, W.L., Chandrasekhar, J., Madura, J.D., Impey, R.W., and Klein, M.L. (1983). Comparison of simple potential functions for simulating liquid water. J. Chem. Phys. *79*, 926–935.

Kandiah, E., Giraud, T., de Maria Antolinos, A., Dobias, F., Effantin, G., Flot, D., Hons, M., Schoehn, G., Susini, J., Svensson, O., et al. (2019). CM01: a facility for cryo-electron microscopy at the European Synchrotron. Acta Crystallogr D Struct Biol *75*, 528–535.

Klauda, J.B., Venable, R.M., Freites, J.A., O'Connor, J.W., Tobias, D.J., Mondragon-Ramirez, C., Vorobyov, I., MacKerell, A.D., Jr, and Pastor, R.W. (2010). Update of the CHARMM all-atom additive force field for lipids: validation on six lipid types. J. Phys. Chem. B *114*, 7830–7843.

Kumar, A., Basak, S., Rao, S., Gicheru, Y., Mayer, M.L., Sansom, M.S.P., and Chakrapani, S. (2020). Mechanisms of activation and desensitization of full-length glycine receptor in lipid nanodiscs. Nat. Commun. *11*, 3752.

Langley, J.N. (1905). On the reaction of cells and of nerve-endings to certain poisons, chiefly as regards the reaction of striated muscle to nicotine and to curari. J. Physiol. *33*, 374–413.

Lape, R., Colquhoun, D., and Sivilotti, L.G. (2008). On the nature of partial agonism in the nicotinic receptor superfamily. Nature *454*, 722–727.

Laverty, D., Thomas, P., Field, M., Andersen, O.J., Gold, M.G., Biggin, P.C., Gielen, M., and Smart, T.G. (2017). Crystal structures of a GABAA-receptor chimera reveal new endogenous neurosteroid-binding sites. Nat. Struct. Mol. Biol. *24*, 977–985.

Laverty, D., Desai, R., Uchański, T., Masiulis, S., Stec, W.J., Malinauskas, T., Zivanov, J., Pardon, E., Steyaert, J., Miller, K.W., et al. (2019). Cryo-EM structure of the human α1β3γ2 GABAA receptor in a lipid bilayer. Nature *565*, 516–520.

Liebschner, D., Afonine, P.V., Baker, M.L., Bunkóczi, G., Chen, V.B., Croll, T.I., Hintze, B., Hung, L.-W., Jain, S., McCoy, A.J., et al. (2019). Macromolecular structure determination using X-rays, neutrons and electrons: recent developments in Phenix. Acta Crystallographica Section D: Structural Biology *75*, 861–877.

MacKerell, A.D., Bashford, D., Bellott, M., Dunbrack, R.L., Evanseck, J.D., Field, M.J., Fischer, S., Gao, J., Guo, H., Ha, S., et al. (1998). All-atom empirical potential for molecular modeling and dynamics studies of proteins. J. Phys. Chem. B *102*, 3586–3616.

Masiulis, S., Desai, R., Uchański, T., Serna Martin, I., Laverty, D., Karia, D., Malinauskas, T., Zivanov, J., Pardon, E., Kotecha, A., et al. (2019). GABAA receptor signalling mechanisms revealed by structural pharmacology. Nature *565*, 454–459.

Mesoy, S., Jeffreys, J., and Lummis, S.C.R. (2019). Characterization of Residues in the 5-HT3 Receptor M4 Region That Contribute to Function. ACS Chem. Neurosci.

Miller, P.S., Scott, S., Masiulis, S., De Colibus, L., Pardon, E., Steyaert, J., and Aricescu, A.R. (2017). Structural basis for GABAA receptor potentiation by neurosteroids. Nat. Struct. Mol. Biol. *24*, 986–992.

Miyamoto, S., and Kollman, P.A. (1992). Settle: An analytical version of the SHAKE and RATTLE algorithm for rigid water models. J. Comput. Chem. *13*, 952–962.

Miyazawa, A., Fujiyoshi, Y., and Unwin, N. (2003). Structure and gating mechanism of the acetylcholine receptor pore. Nature *423*, 949–955.

Mosesso, R., and Dougherty, D.A. (2018). A triad of residues is functionally transferrable between 5-HT3 serotonin receptors and nicotinic acetylcholine receptors. J. Biol. Chem. *293*, 2903–2914.

Mukhtasimova, N., Free, C., and Sine, S.M. (2005). Initial coupling of binding to gating mediated by conserved residues in the muscle nicotinic receptor. J. Gen. Physiol. *126*, 23–39.

Mukhtasimova, N., Lee, W., Wang, H., and Sine, S. (2009). Detection and trapping of intermediate states priming nicotinic receptor channel opening. Nature.

Nayak, T.K., and Auerbach, A. (2013). Asymmetric transmitter binding sites of fetal muscle acetylcholine receptors shape their synaptic response. Proc. Natl. Acad. Sci. U. S. A. *110*, 13654–13659.

Noviello, C.M., Gharpure, A., Mukhtasimova, N., Cabuco, R., Baxter, L., Borek, D., Sine, S.M., and Hibbs, R.E. (2021). Structure and gating mechanism of the α7 nicotinic acetylcholine receptor. Cell.

Oliveira, A.S.F., Shoemark, D.K., Campello, H.R., Wonnacott, S., Gallagher, T., Sessions, R.B., and Mulholland, A.J. (2019). Identification of the Initial Steps in Signal Transduction in the α4β2 Nicotinic Receptor: Insights from Equilibrium and Nonequilibrium Simulations. Structure *27*, 1171–1183.e3.

Pettersen, E.F., Goddard, T.D., Huang, C.C., Couch, G.S., Greenblatt, D.M., Meng, E.C., and Ferrin, T.E. (2004). UCSF Chimera--a visualization system for exploratory research and analysis. J. Comput. Chem. *25*, 1605–1612.

Pettersen, E.F., Goddard, T.D., Huang, C.C., Meng, E.C., Couch, G.S., Croll, T.I., Morris, J.H., and Ferrin, T.E. (2021). UCSF ChimeraX: Structure visualization for researchers, educators, and developers. Protein Sci. *30*, 70–82.

Phillips, J.C., Braun, R., Wang, W., Gumbart, J., Tajkhorshid, E., Villa, E., Chipot, C., Skeel, R.D., Kalé, L., and Schulten, K. (2005). Scalable molecular dynamics with NAMD. J. Comput. Chem. *26*, 1781–1802.

Phillips, J.C., Hardy, D.J., Maia, J.D.C., Stone, J.E., Ribeiro, J.V., Bernardi, R.C., Buch, R., Fiorin, G., Hénin, J., Jiang, W., et al. (2020). Scalable molecular dynamics on CPU and GPU architectures with NAMD. J. Chem. Phys. *153*, 044130.

Polovinkin, L., Hassaine, G., Perot, J., Neumann, E., Jensen, A.A., Lefebvre, S.N., Corringer, P.-J., Neyton, J., Chipot, C., Dehez, F., et al. (2018). Conformational transitions of the serotonin 5-HT3 receptor. Nature *563*, 275–279.

Prince, R.J., and Sine, S.M. (1996). Molecular dissection of subunit interfaces in the acetylcholine receptor. Identification of residues that determine agonist selectivity. J. Biol. Chem. *271*, 25770–25777.

Punjani, A., and Fleet, D.J. (2021). 3D variability analysis: Resolving continuous flexibility and discrete heterogeneity from single particle cryo-EM. J. Struct. Biol. *213*, 107702.

Punjani, A., Rubinstein, J.L., Fleet, D.J., and Brubaker, M.A. (2017). cryoSPARC: algorithms for rapid unsupervised cryo-EM structure determination. Nat. Methods *14*, 290–296.

Punjani, A., Zhang, H., and Fleet, D.J. (2020). Non-uniform refinement: adaptive regularization improves single-particle cryo-EM reconstruction. Nat. Methods *17*, 1214–1221.

Rahman, M.M., Teng, J., Worrell, B.T., Noviello, C.M., Lee, M., Karlin, A., Stowell, M.H.B., and Hibbs, R.E. (2020). Structure of the Native Muscle-type Nicotinic Receptor and Inhibition by Snake Venom Toxins. Neuron *0*.

Rao, S., Klesse, G., Lynch, C.I., Tucker, S.J., and Sansom, M.S.P. (2021). Molecular Simulations of Hydrophobic Gating of Pentameric Ligand Gated Ion Channels: Insights into Water and Ions. J. Phys. Chem. B *125*, 981–994.

Reddy, B., Bavi, N., Lu, A., Park, Y., and Perozo, E. (2019). Molecular basis of force-from-lipids gating in the mechanosensitive channel MscS. Elife *8*.

Rovšnik, U., Zhuang, Y., Axelsson, L., Forsberg, B.O., Lim, V., Carroni, M., Blau, C., Howard, R.J., and Lindahl, E. (2020). Characterization of the dynamic resting state of a pentameric ligand-gated ion channel by cryo-electron microscopy and simulations.

Ryckaert, J.-P., Ciccotti, G., and Berendsen, H.J.C. (1977). Numerical integration of the cartesian equations of motion of a system with constraints: molecular dynamics of n-alkanes. J. Comput. Phys. *23*, 327–341.

Sanchez-Garcia, R., Gomez-Blanco, J., Cuervo, A., Carazo, J.M., Sorzano, C.O.S., and Vargas, J. (2021). DeepEMhancer: a deep learning solution for cryo-EM volume post-processing. Commun Biol *4*, 874.

Shen, X.-M., Brengman, J.M., Shen, S., Durmus, H., Preethish-Kumar, V., Yuceyar, N., Vengalil, S., Nalini, A., Deymeer, F., Sine, S.M., et al. (2018). Mutations causing congenital myasthenia reveal principal coupling pathway in the acetylcholine receptor ε-subunit. JCI Insight *3*.

Sine, S.M., Claudio, T., and Sigworth, F.J. (1990). Activation of Torpedo acetylcholine receptors expressed in mouse fibroblasts. Single channel current kinetics reveal distinct agonist binding affinities. J. Gen. Physiol. *96*, 395–437.

Sine, S.M., Shen, X.-M., Wang, H.-L., Ohno, K., Lee, W.-Y., Tsujino, A., Brengmann, J., Bren, N., Vajsar, J., and Engel, A.G. (2002). Naturally occurring mutations at the acetylcholine receptor binding site independently alter ACh binding and channel gating. J. Gen. Physiol. *120*, 483–496.

Smart, O.S., Neduvelil, J.G., Wang, X., Wallace, B.A., and Sansom, M.S. (1996). HOLE: a program for the analysis of the pore dimensions of ion channel structural models. J. Mol. Graph. *14*, 354–360 – 376.

Strikwerda, J.R., and Sine, S.M. (2021). Unmasking coupling between channel gating and ion permeation in the muscle nicotinic receptor. Elife *10*.

Sun, J., Comeau, J.F., and Baenziger, J.E. (2017). Probing the structure of the uncoupled nicotinic acetylcholine receptor. Biochim. Biophys. Acta Biomembr. *1859*, 146–154.

Thompson, M.J., and Baenziger, J.E. (2020). Structural basis for the modulation of pentameric ligand-gated ion channel function by lipids. Biochim. Biophys. Acta Biomembr. *1862*, 183304.

Thompson, M.J., Domville, J.A., and Baenziger, J.E. (2020). The functional role of the αM4 transmembrane helix in the muscle nicotinic acetylcholine receptor probed through mutagenesis and coevolutionary analyses. J. Biol. Chem. *295*, 11056–11067.

Trick, J.L., Chelvaniththilan, S., Klesse, G., Aryal, P., Wallace, E.J., Tucker, S.J., and Sansom, M.S.P. (2016). Functional Annotation of Ion Channel Structures by Molecular Simulation. Structure.

Tuckerman, M., Berne, B.J., and Martyna, G.J. (1992). Reversible multiple time scale molecular dynamics. J. Chem. Phys. *97*, 1990–2001.

Uchański, T., Masiulis, S., Fischer, B., Kalichuk, V., López-Sánchez, U., Zarkadas, E., Weckener, M., Sente, A., Ward, P., Wohlkönig, A., et al. (2021). Megabodies expand the nanobody toolkit for protein structure determination by single-particle cryo-EM. Nat. Methods *18*, 60–68.

Unwin, N. (2005). Refined structure of the nicotinic acetylcholine receptor at 4A resolution. J. Mol. Biol. *346*, 967–989.

Unwin, N. (2013). Nicotinic acetylcholine receptor and the structural basis of neuromuscular transmission: insights from Torpedo postsynaptic membranes. Q. Rev. Biophys. 1–40.

Unwin, N., and Fujiyoshi, Y. (2012). Gating Movement of Acetylcholine Receptor Caught by Plunge-Freezing. J. Mol. Biol. *422*, 617–634.

Vanommeslaeghe, K., Hatcher, E., Acharya, C., Kundu, S., Zhong, S., Shim, J., Darian, E., Guvench, O., Lopes, P., Vorobyov, I., et al. (2009). CHARMM general force field: A force field for drug-like molecules compatible with the CHARMM all-atom additive biological force fields. Journal of Computational Chemistry NA – NA.

Wagner, T., Merino, F., Stabrin, M., Moriya, T., Antoni, C., Apelbaum, A., Hagel, P., Sitsel, O., Raisch, T., Prumbaum, D., et al. (2019). SPHIRE-crYOLO is a fast and accurate fully automated particle picker for cryo-EM. Commun Biol *2*, 218.

Walsh, R.M., Jr, Roh, S.-H., Gharpure, A., Morales-Perez, C.L., Teng, J., and Hibbs, R.E. (2018). Structural principles of distinct assemblies of the human α4β2 nicotinic receptor. Nature *557*, 261–265.

Williams, C.J., Headd, J.J., Moriarty, N.W., Prisant, M.G., Videau, L.L., Deis, L.N., Verma, V., Keedy, D.A., Hintze, B.J., Chen, V.B., et al. (2018). MolProbity: More and better reference data for improved all-atom structure validation. Protein Sci. *27*, 293–315.

Wilson, G.G., and Karlin, A. (2001). Acetylcholine receptor channel structure in the resting, open, and desensitized states probed with the substituted-cysteine-accessibility method. Proceedings of the National Academy of Sciences *98*, 1241–1248.

Wiltfong, R.E., and Jansen, M. (2009). Probing protein packing surrounding the residues in and flanking the nicotinic acetylcholine receptor M2M3 loop. J. Neurosci. *29*, 1626–1635.

Wu, E.L., Cheng, X., Jo, S., Rui, H., Song, K.C., Dávila-Contreras, E.M., Qi, Y., Lee, J., Monje-Galvan, V., Venable, R.M., et al. (2014). CHARMM-GUI Membrane Builder toward realistic biological membrane simulations. J. Comput. Chem. *35*, 1997–2004.

Xiu, X., Puskar, N.L., Shanata, J.A.P., Lester, H.A., and Dougherty, D.A. (2009). Nicotine binding to brain receptors requires a strong cation-pi interaction. Nature *458*, 534–537.

Zarkadas, E., Zhang, H., Cai, W., Effantin, G., Perot, J., Neyton, J., Chipot, C., Schoehn, G., Dehez, F., and Nury, H. (2020). The binding of palonosetron and other antiemetic drugs to the serotonin 5-HT3 receptor.

Zhang, Y., Chen, J., and Auerbach, A. (1995). Activation of recombinant mouse acetylcholine receptors by acetylcholine, carbamylcholine and tetramethylammonium. J. Physiol. *486 (Pt 1)*, 189–206.

Zheng, S.Q., Palovcak, E., Armache, J.-P., Verba, K.A., Cheng, Y., and Agard, D.A. (2017). MotionCor2: anisotropic correction of beam-induced motion for improved cryo-electron microscopy. Nat. Methods *14*, 331–332.

Zhong, W., Gallivan, J.P., Zhang, Y., Li, L., Lester, H.A., and Dougherty, D.A. (1998). From ab initio quantum mechanics to molecular neurobiology: a cation-pi binding site in the nicotinic receptor. Proc. Natl. Acad. Sci. U. S. A. *95*, 12088–12093.

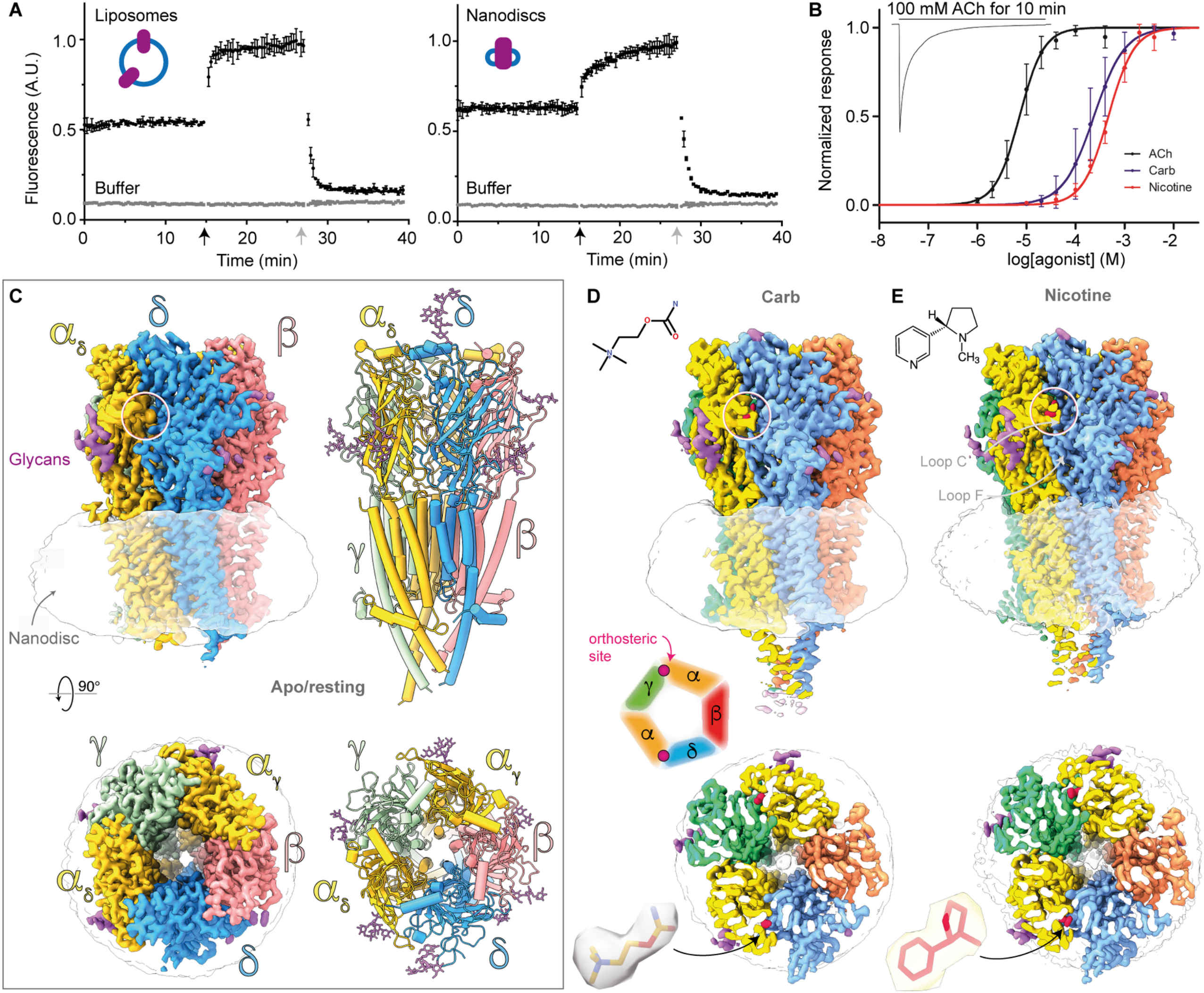
A
Liposomes
Fluorescence (A.U.)
1.0
0.5
0.0
Buffer
0
10
20
30
40
Time (min)
Nanodiscs
1.0
0.5
0.0
Buffer
0
10
20
30
40
Time (min)
B
100 mM ACh for 10 min
Normalized response
1.0
0.5
0.0
-8
-7
-6
-5
-4
-3
-2
log[agonist] (M)
ACh
Carb
Nicotine
C
δ
α_δ
β
Glycans
Nanodisc
α_δ
δ
γ
β
90°
Apo/resting
γ
α_γ
α_δ
β
δ
γ
α_γ
β
α_δ
δ
D
Carb
N
O
O
N
orthosteric site
γ
α
β
α
δ
E
Nicotine
H
N
N
CH_3
Loop C
Loop F

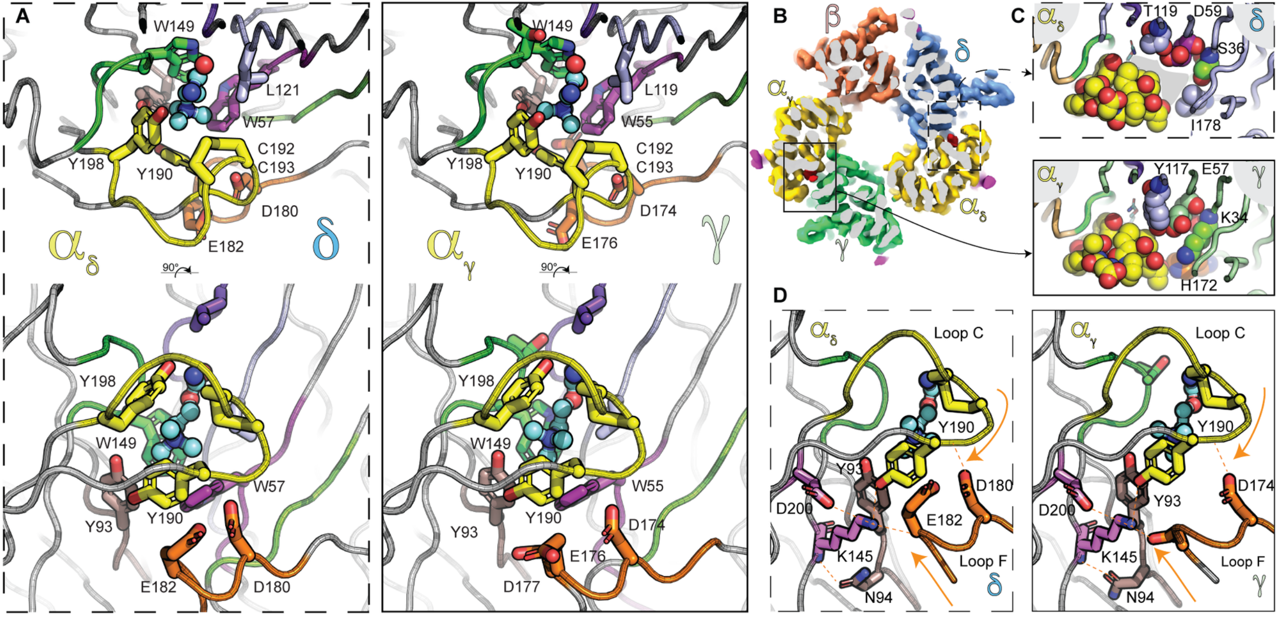
A
W149
L121
W57
Y198
Y190
C192
C193
D180
E182
α_δ
δ
90°
Y198
W149
W57
Y93
Y190
E182
D180
W149
L119
W55
Y198
Y190
C192
C193
D174
E176
α_γ
γ
90°
Y198
W149
W55
Y93
Y190
D174
E176
D177
B
β
δ
α_γ
α_δ
γ
C
α_δ
T119
D59
δ
S36
I178
α_γ
Y117
E57
γ
K34
H172
D
α_δ
Loop C
Y190
Y93
D180
D200
E182
K145
Loop F
N94
δ
α_γ
Loop C
Y190
D174
D200
Y93
K145
Loop F
N94
γ

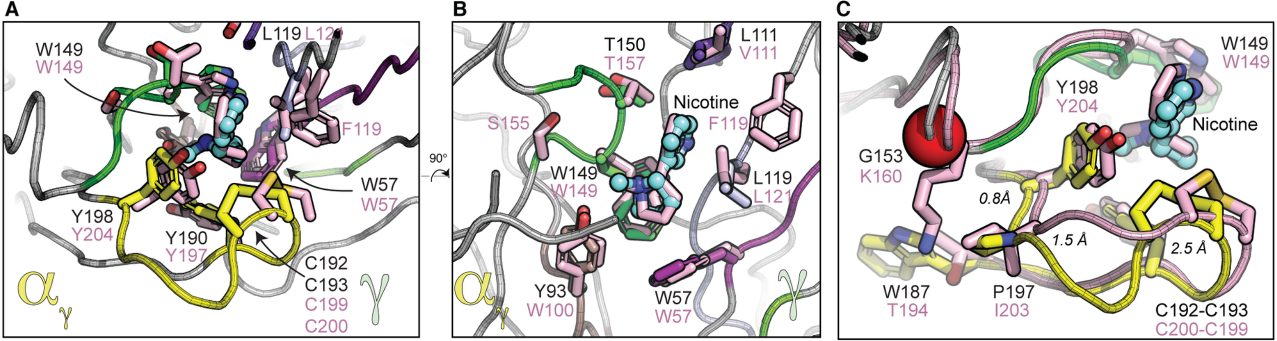
A
W149
W149
L119 L121
F119
W57
W57
Y198
Y204
Y190
Y197
C192
C193
C199
C200
α
γ
γ
90°
B
T150
T157
L111
V111
Nicotine
S155
F119
W149
W149
L119
L121
Y93
W100
W57
W57
α
γ
γ
C
W149
W149
Y198
Y204
Nicotine
G153
K160
0.8Å
1.5 Å
2.5 Å
W187
T194
P197
I203
C192-C193
C200-C199

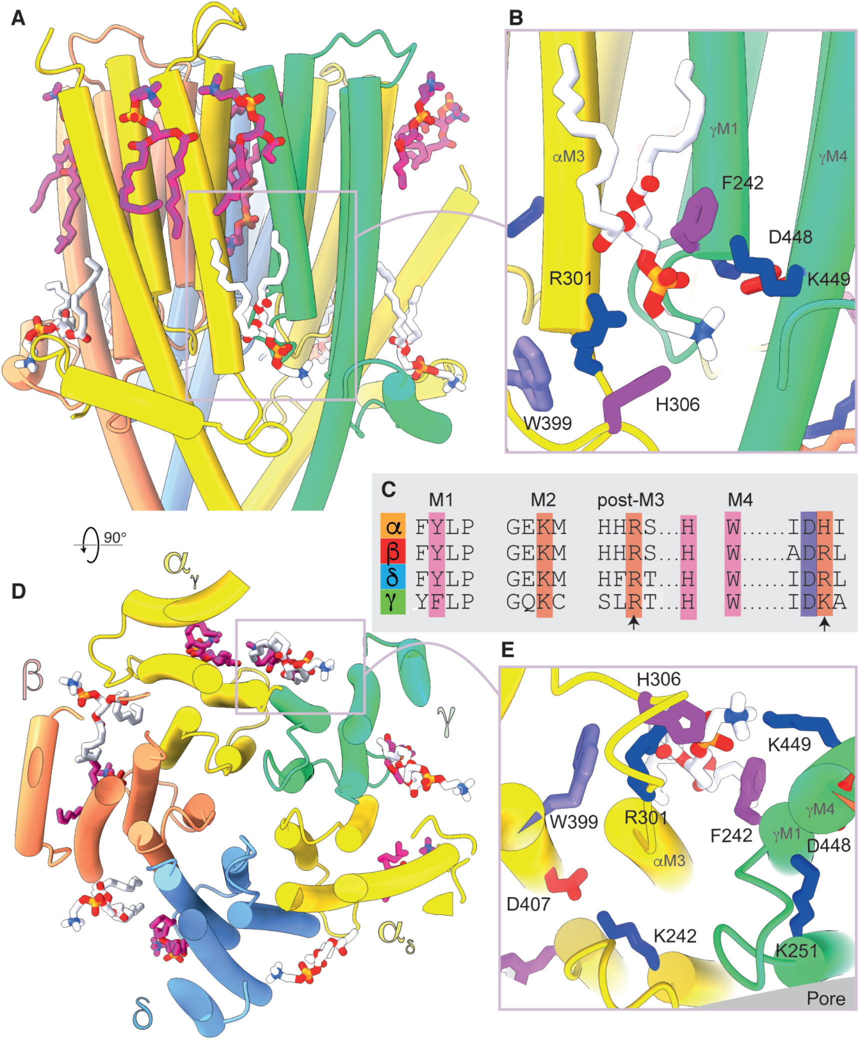
A
B
αM3
γM1
γM4
F242
D448
R301
K449
H306
W399
C
M1
M2
post-M3
M4
α FYLP GEKM HHRS...H W......IDHI
β FYLP GEKM HHRS...H W......ADRL
δ FYLP GEKM HFRT...H W......IDRL
γ YFLP GQKC SLRT...H W......IDKA
90°
D
α_γ
β
γ
δ
α_δ
E
H306
K449
W399
R301
F242
γM4
γM1
D448
αM3
D407
K242
K251
Pore

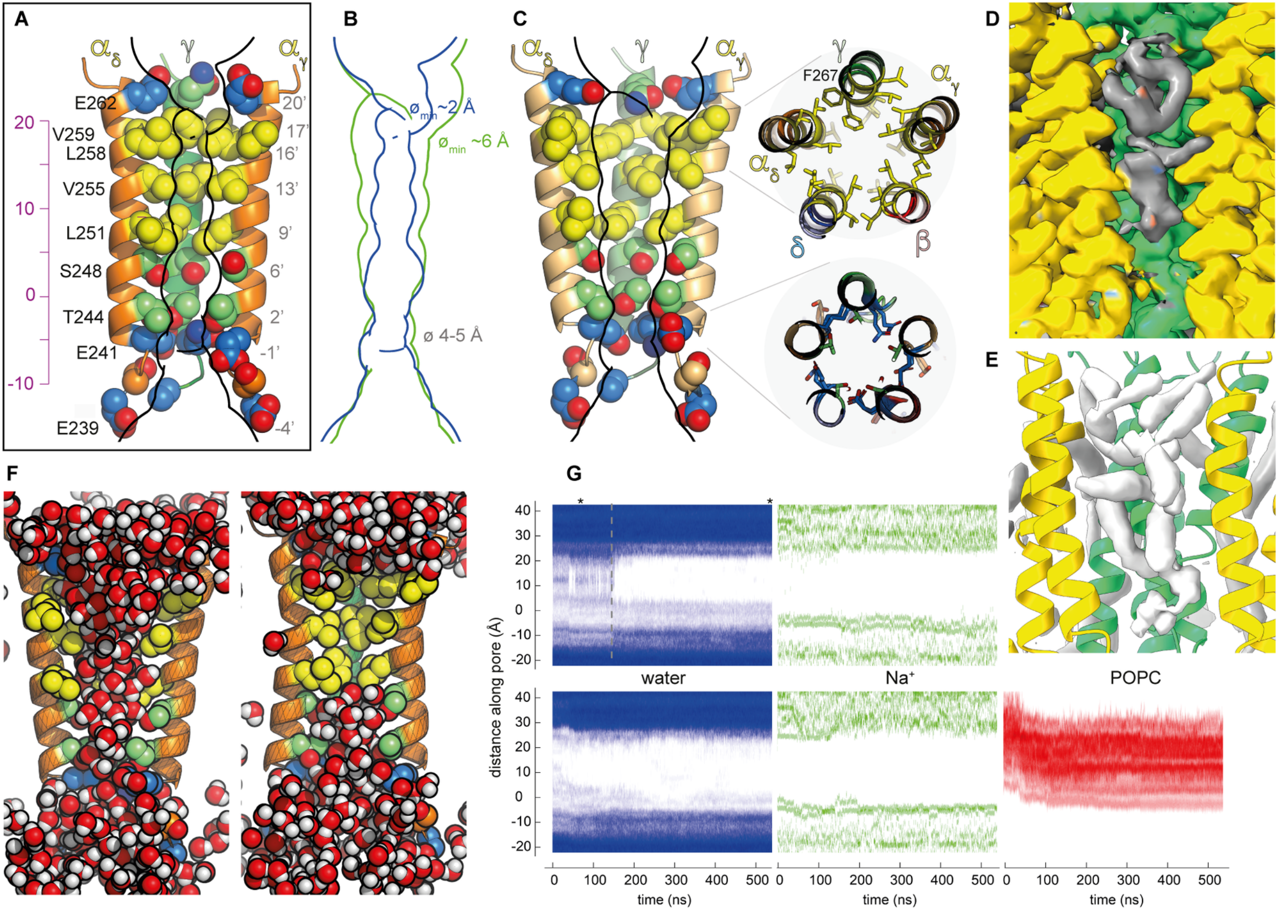
A
αδ
γ
αγ
E262
20'
20
V259
17'
L258
16'
V255
13'
10
L251
9'
S248
6'
0
T244
2'
E241
-1'
-10
E239
-4'
B
ømin ~2 Å
ømin ~6 Å
ø 4-5 Å
C
αδ
γ
αγ
γ
F267
αγ
αδ
δ
β
D
E
F
G
*
*
40
30
20
10
0
-10
-20
distance along pore (Å)
water
Na+
POPC
0
100
200
300
400
500
time (ns)

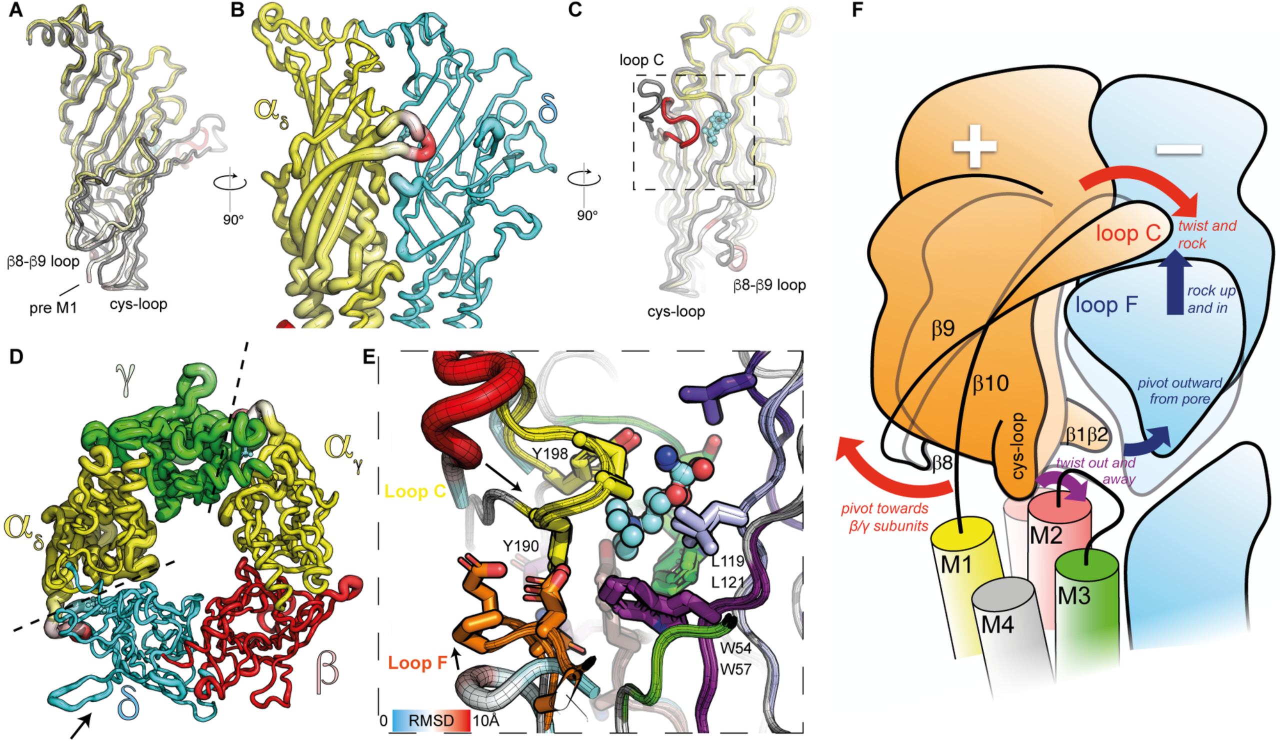
A
β8-β9 loop
pre M1
cys-loop
90°
B
α_δ
δ
90°
C
loop C
β8-β9 loop
cys-loop
D
γ
α_γ
α_δ
δ
β
E
Y198
Loop C
Y190
L119
L121
W54
W57
Loop F
0 RMSD 10Å
F
+
−
loop C
twist and rock
rock up and in
loop F
β9
β10
pivot outward from pore
cys-loop
β1β2
β8
twist out and away
pivot towards β/γ subunits
M1
M2
M3
M4

Structural basis for agonist binding and channel activation in a muscle acetylcholine receptor